

# 1 A 250m annual alpine grassland AGB dataset over the Qinghai- 2 Tibetan Plateau (2000-2019) in China based on in-situ measurements, 3 UAV images, and MODIS Data

4 Huifang Zhang<sup>1,2,3</sup>, Zhonggang Tang<sup>2</sup>, Binyao Wang<sup>2</sup>, Hongcheng Kan<sup>2</sup>, Yi Sun<sup>1,2</sup>, Yu Qin<sup>3</sup>, Baoping  
5 Meng<sup>1,2</sup>, Meng Li<sup>1,2</sup>, Jianjun Chen<sup>4</sup>, Yanyan Lv<sup>1,2</sup>, Jianguo Zhang<sup>1,2</sup>, Shuli Niu<sup>5</sup>, Shuhua Yi<sup>1,2,\*</sup>

6  
7 <sup>1</sup>Institute of Fragile Eco-environment, Nantong University, 999 Tongjing Road, Nantong, Jiangsu, 226007, China

8 <sup>2</sup>School of Geographic Science, Nantong University, 999 Tongjing Road, Nantong, Jiangsu, 226007, China

9 <sup>3</sup>State Key Laboratory of Cryospheric Sciences, Northwest Institute of Eco-Environment and Resources, Chinese Academy  
10 of Sciences, 320 Donggang West Road, Lanzhou 730000, China

11 <sup>4</sup>College of Geomatics and Geoinformation, Guilin University of Technology, 12 Jiangan Road, Guilin 541004, China;

12 <sup>5</sup>Key Laboratory of Ecosystem Network Observation and Modeling, Institute of Geographic Sciences and Natural Resources  
13 Research, Chinese Academy of Sciences, Beijing, China

14

15 *Correspondence to:* Shuhua Yi ([wis@ntu.edu.cn](mailto:wis@ntu.edu.cn))

16 **Abstract.** The alpine grassland ecosystem accounts for 53% of the Qinghai-Tibet Plateau (QTP) area and is an important  
17 ecological protection barrier, but it is fragile and vulnerable to climate change. Therefore, continuous monitoring of  
18 grassland aboveground biomass (AGB) is necessary. Although many studies have mapped the spatial distribution of AGB  
19 for QTP, the results vary widely due to the limited ground samples and mismatch with satellite pixel scales. This paper  
20 proposed a new algorithm using unmanned aerial vehicles (UAVs) as a bridge to re-estimate the grassland AGB on the QTP  
21 from 2000 to 2019. The innovations were as follows: 1) In terms of ground data acquisition, the spatial scale matching  
22 among the traditional ground samples, UAV photos, and MODIS pixels was considered. During 2015-2019, 906 pairs of  
23 quadrat-scale ground-UAV sample data and 2,602 sets of MODIS pixel-scale UAV data were collected (over 37,000 UAV  
24 photos). Therefore, the ground validation samples were sufficient and scale-matched. 2) In terms of model construction, the  
25 traditional quadrat scale (0.25m<sup>2</sup>) was successfully upscaled to the MODIS pixel scale (6,2500 m<sup>2</sup>) based on the random  
26 forest and stepwise upscaling methods. Compared with previous studies, the scale matching of independent and dependent  
27 variables was achieved, effectively reducing the impact of spatial scale mismatch. The results showed that the correlation  
28 between the AGB values estimated by UAV and the MODIS vegetation indices was higher than that of the traditional  
29 sampling method at the pixel scale. The cross-year validation results showed that the constructed pixel scale AGB estimation  
30 had good robustness, with an average R<sup>2</sup> of 0.83 and RMSE of 34.13 g/m<sup>2</sup>. Our dataset provides an important input  
31 parameter for a comprehensive understanding of the role of QTP in global climate change processes. The dataset is available  
32 from the National Tibetan Plateau/Third Pole Environment Data Center (<https://doi.org/10.11888/Terre.tpdc.272587>, Zhang  
33 et al., 2022).

## 34 **1 Introduction**

35 Grasslands, accounting for approximately 37% of the earth's surface, play an essential role in global carbon cycling and food  
36 supply (O'mara, 2012). However, most natural grasslands have been degraded to a certain extent due to overgrazing,  
37 farmland encroachment, soil erosion, and global climate change (Suttie et al., 2005; Ramankutty et al., 2008; O'mara, 2012).  
38 Therefore, timely monitoring of grassland health is crucial for sustainable development and understanding global carbon  
39 cycling processing. Aboveground biomass (AGB) is a key indicator of grassland status and an important input parameter for  
40 ecological modeling and carbon storage estimation. Thus, accurate and rapid estimation of AGB is valuable for grassland  
41 monitoring.

42

43 The advent of satellites has made it possible to map the spatiotemporal dynamics of grasslands over large areas. Spectral  
44 information from different satellites has been employed for biomass estimation, such as Sentinel-2, Landsat, and MODIS  
45 (Wang et al., 2019; Zhang et al., 2016). Although there are differences in spatial and spectral resolution, the core idea of  
46 building a biomass model is constructing the linear or nonlinear relationships between the field-measured samples and  
47 various satellite spectral indices. Therefore, the estimation accuracy is closely related to the quality and quantity of ground  
48 samples (Morais et al., 2021; Yu et al., 2021). However, there are still two deficiencies in ground data acquisition: the large  
49 spatial gap between the traditional samples and satellite pixels, and the low efficiency.

50

51 How to narrow the spatial gap between traditional samples and satellite pixels is an urgent problem to be solved. Since it is  
52 impossible to harvest all grasses within a pixel range, the average of 3-5 quadrats ( $0.5\text{ m} \times 0.5\text{ m}$  or  $1\text{ m} \times 1\text{ m}$ ) is usually used  
53 as the measurement (Dusseux et al., 2015; Yang et al., 2017), which results in a considerable spatial gap. A lot of studies  
54 have been carried out to upscale ground measurements to satellite pixels (Crow et al., 2012; Bian and Walsh, 1993), such as  
55 block Kriging geostatistical interpolation, different types of regression models, or machine learning algorithms (Cheng et al.,  
56 2007; Wang et al., 2014; Cannavacciuolo et al., 1998; Dancy et al., 1986; Li et al., 2018). However, the accuracy of these  
57 methods depends on the density of sampling points. In addition, fine-resolution satellites were used as a bridge to reduce the  
58 impact of scale mismatch on AGB estimation (Yu et al., 2021; He et al., 2019). The reason is that the finer the satellite  
59 resolution, the smaller the spatial gap with the ground samples (Wang and Sun, 2014; Morais et al., 2021). Therefore,  
60 obtaining ground samples that match the pixel scale is the key to improving the accuracy of satellite AGB estimation.

61

62 Improving the efficiency of ground sampling is another issue that needs to be addressed. Although the traditional sampling  
63 method can yield high-accuracy results, it is time-consuming and labor-intensive. For example, Yang et al. spent five years  
64 completing the collection of ground samples to invert the grassland AGB in China (Yang et al., 2010). Moreover, with  
65 limited original ground data, some scholars had to use the data published by others to expand the sample size (Xia et al.,

66 2018; Jiao et al., 2017). However, datasets from different sources may affect the overall accuracy due to the differences in  
67 sample plot size, sample size, and sampling methods.

68

69 The development and popularity of unmanned aerial vehicle (UAV) technology has provided new solutions to the above  
70 problems. UAV images have been successfully used to estimate ecological metrics such as FVC, biomass, and canopy height  
71 (Chen et al., 2016; Zhang et al., 2018; Bendig et al., 2015). The use of UAVs has the following unparalleled advantages over  
72 traditional sampling methods. First, UAVs can effectively obtain two- or three-dimensional vegetation information in a non-  
73 destructive way, which is helpful for grassland estimation (Lussem et al., 2019; Zhang et al., 2022a; Zhang et al., 2018).  
74 Second, UAVs can rapidly collect key parameters of grassland within satellite pixels (e.g., FVC, Chen et al. 2016). Hence,  
75 UAV images can serve as a bridge to reduce the spatial gap between field samples and satellite pixels. However, most  
76 current UAV-based grassland biomass estimations are small-scale, with few regional-scale studies. Whether UAVs can be  
77 used to reduce the spatial gap between traditional ground sampling and satellite pixels remains an open question. In addition,  
78 previous studies lacked cross-year validation to test the robustness of the AGB estimation model over time due to the limited  
79 sample size.

80

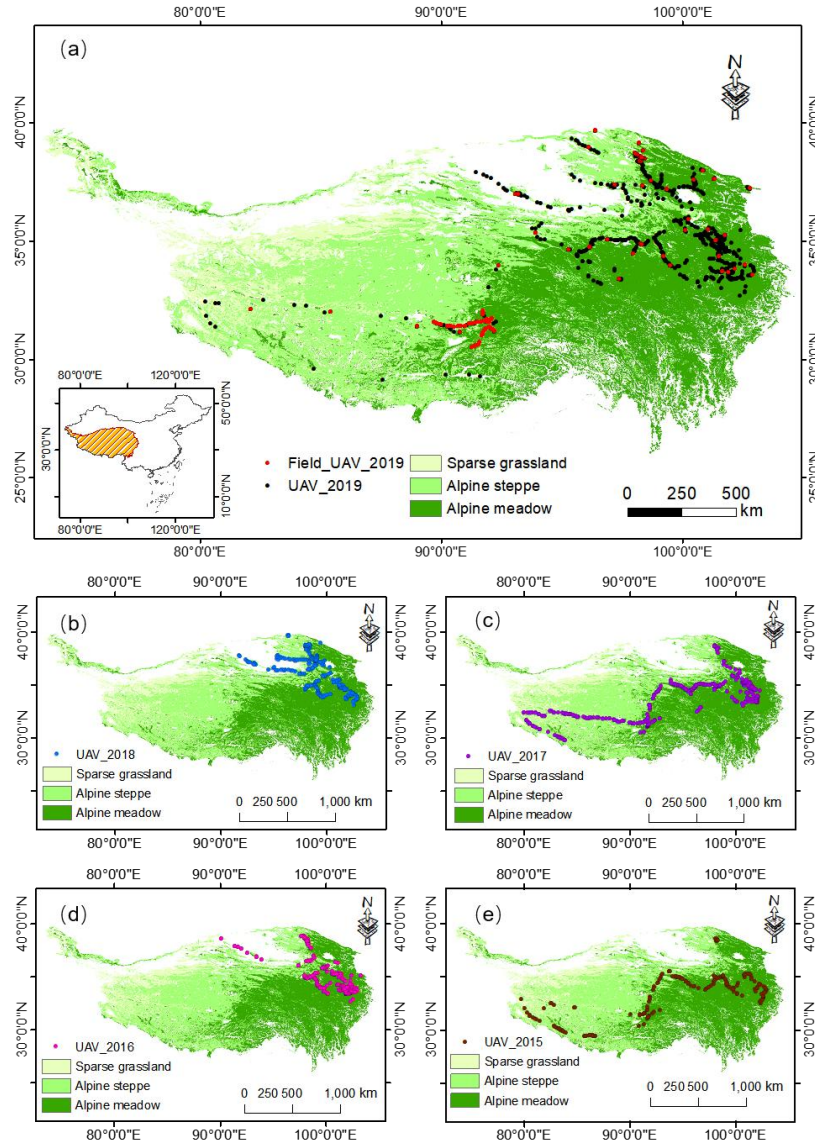
81 This study proposed a new approach that combines traditional ground sampling, UAV photography, and satellite data to  
82 produce a new reliable AGB dataset of QTP grassland. The objectives of this study were: 1) to construct a UAV-based  
83 grassland AGB estimation model at the quadrat/satellite pixel scales, respectively; 2) to investigate whether UAVs can be  
84 used as a bridge to reduce the spatial gap between ground samples and satellite pixels to improve the accuracy of grassland  
85 AGB, and 3) to map the AGB of alpine grasslands on the Qinghai-Tibetan Plateau (QTP) from 2000 to 2019.

## 86 **2 Materials and Methods**

### 87 **2.1 Study Site**

88 QTP is the highest and largest plateau on the earth (26°00'12"~39°46'50"N, 73°18'52"~104°46'59"E), with an average  
89 elevation of ~4000 m and an area of approximately  $257.24 \times 10^4$  km<sup>2</sup> (Figure 1). It is located in western China, with an  
90 average annual temperature and precipitation of about 1.6°C and 413.6 mm, respectively. The main grassland types are  
91 alpine meadows, alpine steppe, and sparse grassland, which play a critical role in climate regulation, water conservation, and  
92 biodiversity protection (Ding et al., 2013). In this study, the boundary of the QTP of China (Zhang et al., 2014) was  
93 downloaded from the National Earth System Science Data Center, National Science & Technology Infrastructure of China  
94 (<http://www.geodata.cn>). Grassland type data was derived from the 1:1000000 Chinese digital grassland classification map  
95 provided by the China Resource and Environmental Science and Data Center (<https://www.resdc.cn/>). This data set,  
96 generated through field surveys in the 1980s and supplemented by satellite and aerial imagery, is the most detailed

97 grassland-type map available. For comparison with others, we combined the grassland types into three categories: alpine  
98 meadow, alpine grassland, and sparse grassland, and resampled to 250 m (Table A1).



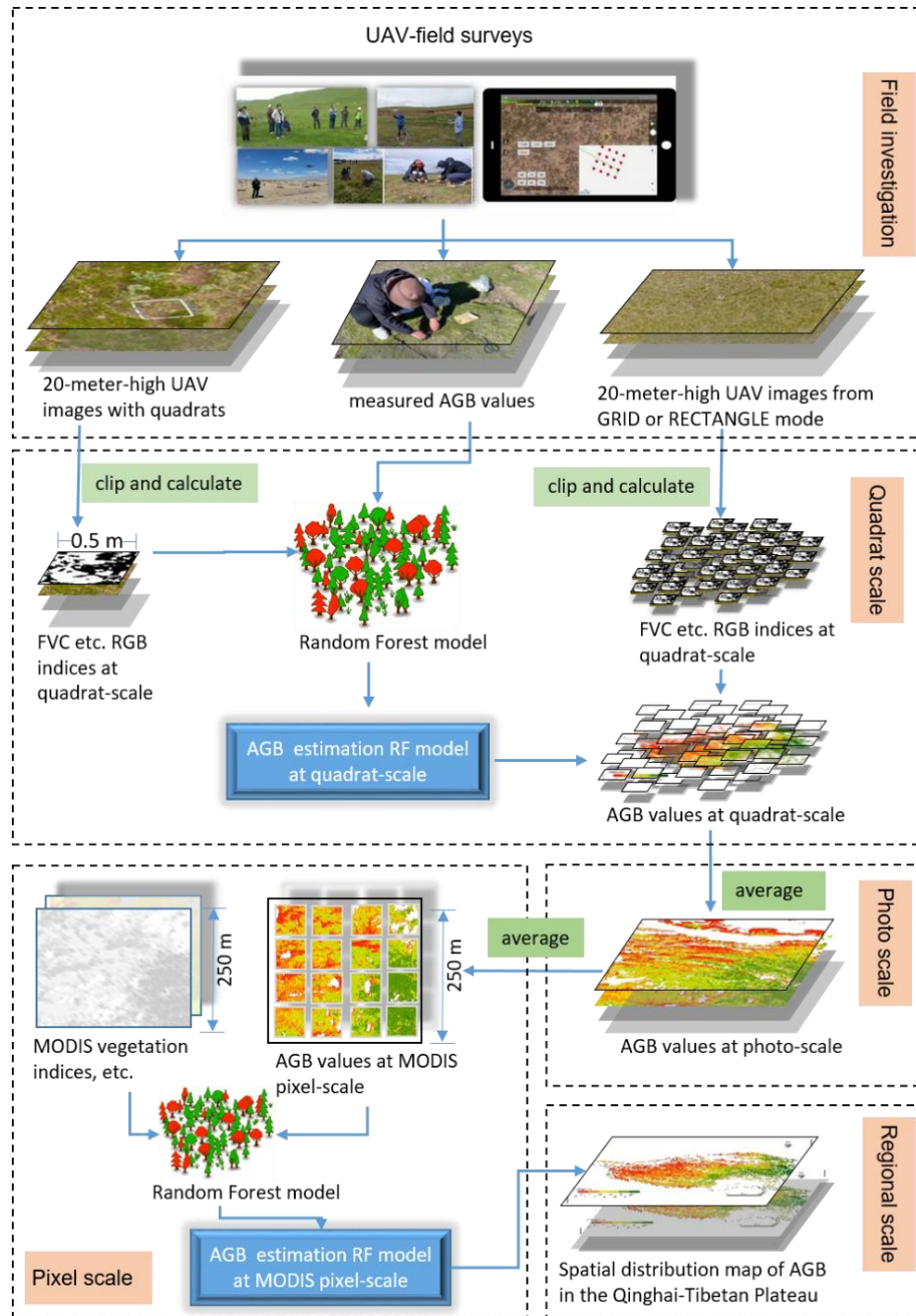
99

100 **Figure 1. Distribution of field and UAV sampling sites in 2019 (a); UAV sampling sites in alpine grasslands on the QTP from 2015-**  
101 **2018 (b-e). Field\_UAV\_2019 represents the quadrat-scale sampling sites for the 2019 UAV-Field synchronous grassland biomass**  
102 **experiment. UAV\_year represents the UAV sampling point based on the GRID or RECTANGLE mode of the corresponding year.**

## 103 2.2 Overall technology roadmap

104 Figure 2 was the overall flowchart of this study. It consisted of four main steps: 1) UAV and field investigation; 2)  
105 constructing the AGB estimation model at the quadrat scale; 3) upscaling the grassland AGB to the MODIS pixel scale; 4)

106 building the AGB estimation model at the MODIS pixel scale and applying it to the QTP region. More detailed information  
 107 on each step was described in the following sections.



108  
 109  
 110 **Figure 2. The overall flowchart of UAV field survey and the construction of grassland AGB estimation models at different spatial**  
 111 **scales.**

## 112 2.3 Field investigation

### 113 2.3.1 UAV and route planning

114 DJI Phantom 3 Professional (DJI Company, Shenzhen, China), a popular consumer quadrotor UAV with a high-resolution  
115 RGB camera, was used to collect UAV images of the QTP from 2015 to 2019. It has a 1/23-inch CMOS sensor and is  
116 capable of taking 12-megapixel photos. In addition, it uses a 3-axis stable gimbal to take photos vertically downward to  
117 eliminate the distortion of UAV images. It has good environmental adaptability, with an operating temperature range from 0°  
118 to 40°, and a maximum take-off altitude of 6000 meters. Therefore, it is well adapted to the low temperature and high  
119 altitude of the QTP. More detailed information about the UAV system was listed in Table A2.

120

121 Fragmentation Monitoring and Analysis with aerial Photography (FragMap) system, capable of long-term collaborative  
122 observation, was used for UAV route planning (Yi, 2017). During 2015-2019, we conducted UAV monitoring of the QTP  
123 grasslands using FragMap (Figure 1). Over 2,000 fixed flight routes were set up during this period, and more than 37,000  
124 UAV images were collected, providing a reliable UAV dataset for this study (Table 1).

125

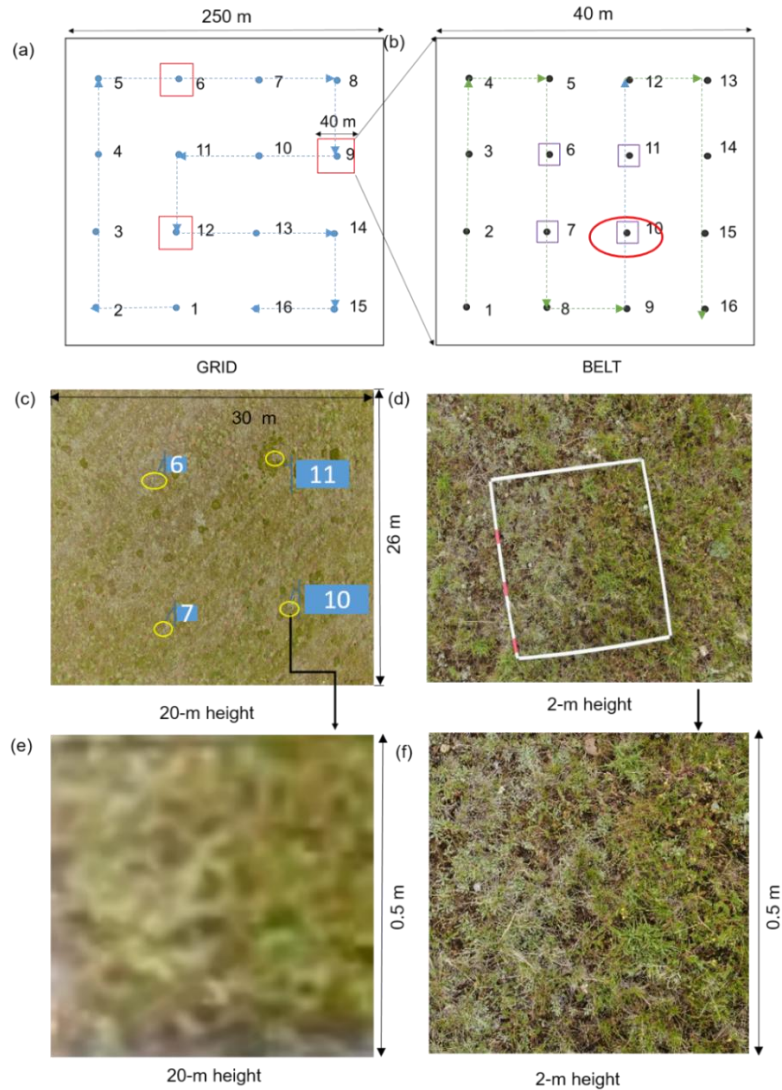
126 **Table 1. UAV sampling information from 2015 to 2019**

<b>Year</b>	<b>Flight Mode</b>	<b>Number of routes</b>	<b>Photo number</b>	<b>Acquisition time</b>
2015	RECTANGLE	214	2568	7.05 ~8.24
2016	RECTANGLE	334	4008	6.20~9.29
	GRID	150	2400	6.20~9.23
2017	RECTANGLE	315	3780	5.10~10.24
	GRID	322	5152	7.15~8.22
2018	RECTANGLE	79	948	7.22~8.03
	GRID	303	4848	7.04~8.29
2019	GRID	885	14160	7.12~9.21
	<b>Total</b>	<b>2602</b>	<b>37864</b>	

127

128 GRID, RECTANGLE, and BELT are the most commonly used flight modes in the FragMap software. GRID and  
129 RECTANGLE modes have 16 and 12 waypoints for capturing UAV images within a MODIS pixel range (Figure A1). Their  
130 flying height and speed are set to 20 m and 3m/s, respectively. The spatial coverage of a 20-meter-high UAV photo is about  
131 26 m × 35 m. The BELT mode is similar to GRID, but is designed to obtain near-ground UAV image data with higher  
132 resolution (Figure 3b). It can be combined with the traditional sampling method to ensure the consistency of UAV images

133 with the ground samples (Figure 3d). Typically, the BELT size is set to 40 m × 40 m, and the flying height and speed are set  
 134 to 2 m and 1 m/s to ensure that field crews have enough time to place sampling frames under the UAV waypoints. As with  
 135 the GRID mode, 16 UAV images can be captured in a single flight. Compared with the MOSAIC flight mode (which  
 136 requires a guaranteed overlap rate between photos to obtain a full view of an area), our design is more in line with the  
 137 traditional ecological sampling concept. It allows for a better balance of spatial representation and accessibility of samples,  
 138 resulting in efficient sample collection.



139  
 140 **Figure 3. Schematic diagram of the UAV-field synchronization experiment in 2019: a combination design of GRID (a) and BELT**  
 141 **(b) flight modes; a UAV image with a quadrat from the BELT mode at the height of 2 m (d); a 20-meter-high UAV image**  
 142 **including four sample quadrats (c); and the cropped UAV images at quadrat scale from 20 m (e) and 2 m (f) height, respectively.**

### 143 2.3.2 Synchronization experiment of UAV and field sampling

144 A UAV-field biomass synchronization experiment was designed in 2019 to ensure spatial matching among satellites, UAVs,  
145 and ground sampling (Figure 3). The specific implementation steps were as follows. First, we set a GRID flight mode with a  
146 MODIS pixel size (250 m × 250 m) (Figure 3a). Then, three waypoints were randomly selected from the GRID mode to set  
147 the BELT flight modes (40 m × 40 m). For each BELT, a sampling frame (0.5 m × 0.5 m) was placed at its 6, 7, 10, and 11  
148 waypoints to ensure that the GRID image could contain the four frames mentioned above (Figure 3b-c). Then, at the end of  
149 all flights, the grassland AGB samples were cut, bagged, and numbered. Finally, these samples were oven-dried at 65°C to  
150 constant weight to obtain the field-measured AGB values.

151

## 152 2.4 Data processing

### 153 2.4.1 UAV photo pre-processing and indices calculation

154 Pre-processing of UAV photos included image quality inspection, cropping, and calculation of different indices. First, we  
155 eliminated overexposed or blurred 20-meter-high UAV images. Second, the pixels in the sampling frames were cropped and  
156 saved (Figure 3e). Third, the RGB indices for the cropped UAV images were calculated. Similar to our previous study,  
157 indices included color space, histogram, and vegetation indices, the details of which can be found in Zhang et al. (2022a). In  
158 addition, 30 other RGB vegetation indices were added as candidate independent variables. The names, formulas, and  
159 references of the above indices were shown in Table A3.

### 160 2.4.2 MODIS vegetation index and other spatial data

161 The MOD13Q1(v006) product was downloaded from the NASA earth explorer website (<https://earthexplorer.usgs.gov/>) for  
162 inversion of the alpine grassland AGB on the QTP. The data contained two commonly used vegetation indices, the  
163 Normalized Vegetation Index (NDVI) and the Enhanced Vegetation Index (EVI), with spatial and temporal resolutions of  
164 250 m and 16 days, respectively. A total of 2,842 scenes from 2000 to 2019 were downloaded. Then, the MODIS images  
165 were reprojected and stitched using the MODIS Projection Tool (MRT). After that, the corresponding vegetation indices  
166 closest to the time of the UAV sampling were extracted to construct/validate a pixel-scale AGB estimation model. In  
167 addition, the kNDVI index was calculated to overcome the NDVI saturation issue based on the equation  $kNDVI = \tanh(NDVI^2)$   
168 (Camps-Valls et al., 2021). The annual maximum vegetation indices were calculated by the maximum value  
169 composition (MVC) algorithm to estimate the spatial AGB distribution of QTP from 2000 to 2019 (Holben, 1986; Wang et  
170 al., 2021; Gao et al., 2020).

171

172 Furthermore, meteorological, soil texture and topographic data were also included as candidate independent variables for  
173 constructing the pixel-scale AGB estimation model. Meteorological factors, including annual mean temperature (TA), annual



174 mean precipitation (PREC), and annual total solar radiation (RAD), were calculated based on the daily meteorological  
175 dataset from the National Meteorological Information Center of China. The data processing steps mainly included  
176 interpolation, cumulative summation, and annual averaging to obtain a meteorological raster dataset with a spatial resolution  
177 of 1000 meters (Li et al., 2021). Moreover, soil texture data at 1 km spatial resolution, including the ratio of soil organic  
178 matter (SOM), clay, sand, and silt, were downloaded from the Resource and Science and Data Center of China  
179 (<https://www.resdc.cn/>). All the meteorological and soil datasets were resampled into 250 m by ArcGIS software to match  
180 the MODIS data.

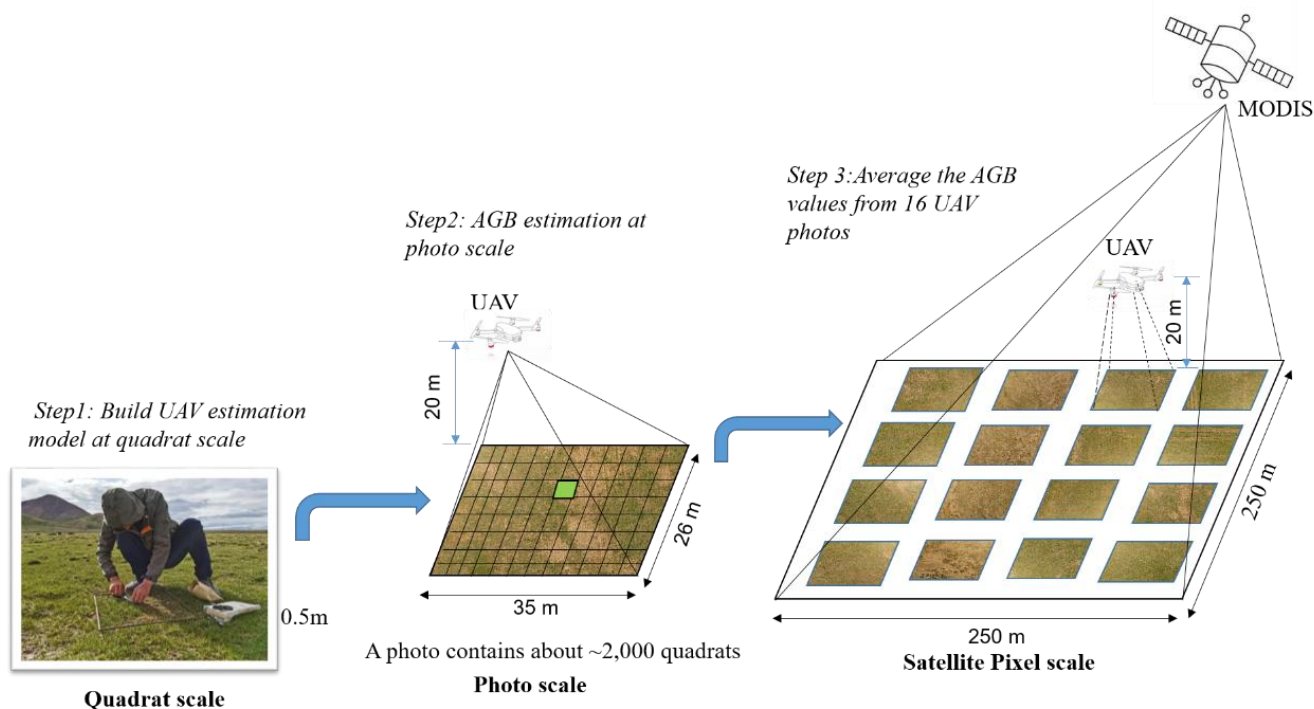
181

182 Terrain factors included the digital elevation model (DEM), slope, and aspect. The DEM was derived from Shuttle Radar  
183 Topography Mission (SRTM) imagery (version 004, 90 m) and resampled to 250 m. The slope and aspect data were derived  
184 from DEM data using the terrain analysis tool of ArcGIS software.

### 185 2.5 AGB modeling and computation at different scales

186 We estimated the grassland AGB at three scales: the quadrat scale, the photo scale, and the satellite pixel scale (Figure 4).

187 More detailed information was described as follows.



188

189 **Figure 4. Upscaling steps to estimate grassland AGB matching the MODIS pixel scale.**

## 190 2.5.1 Modeling method

191 Random Forest (RF) (Breiman, 2001) is an ensemble-learning algorithm that has been widely used to estimate AGB due to  
192 its excellent performance (Ghosh and Behera, 2018; Mutanga et al., 2012; Wang et al., 2016). The two main parameters,  
193 namely the number of regression trees in the forest (*ntree*) and the number of feature variables required to create branches  
194 (*mtry*), were first optimized based on the root mean square error (RMSE) of training data. Here, the value of *ntree* was set  
195 from 100 to 5000 with an interval of 100, while *mtry* was set as the square root of the number of training sample features. In  
196 addition, the importance of each predictor was ranked by calculating the percentage increase in mean square error  
197 (%IncMSE).

198

199 The backward feature elimination method (BFE) was used to reduce the number of input variables to simplify the RF model  
200 (Vergara and Estévez, 2014). The main steps were as follows: 1) constructing an AGB RF model by including all predictor  
201 variables in the initial stages and calculating the %IncMSE index for each variable; 2) eliminating the least promising  
202 variable and then rerunning the RF model until only one independent variable was left. Moreover, the corresponding  
203 coefficient of determination ( $R^2$ ) and the corresponding RMSE were calculated in each iteration; 3) the smallest subset of  
204 variables with the highest  $R^2$  was selected as the final optimized indices.

205

206 In addition, different training and validation strategies were used at different scales. At the quadrat scale, a 10-fold cross-  
207 validation method was used due to the limited ground samples (Kohavi, 1995). At the pixel scale, 30% of the UAV-  
208 estimated AGB samples in 2019 were randomly selected as an independent validation dataset due to the large sample size.  
209 Meanwhile, the UAV\_AGB values from 2015 to 2018 were used for cross-year validation to test the robustness of the model  
210 over time. Statistical metrics  $R^2$  (Eq.1) and RMSE (Eq.2) were used to evaluate the performance of the model.

211

$$R^2 = 1 - \frac{\sum_{i=1}^n (\hat{y}_i - y_i)^2}{\sum_{i=1}^n (\hat{y}_i - \bar{y})^2} \quad (1)$$

212

$$RMSE = \sqrt{\frac{\sum_{i=1}^n (\hat{y}_i - y_i)^2}{n}} \quad (2)$$

213 where  $n$  is the number of samples,  $y_i$  and  $\hat{y}_i$  represent the measured and the predicted AGB value, respectively,  $\bar{y}$  is the  
214 mean value of measured AGB samples.

## 215 2.5.2 AGB RF estimation model at the quadrat scale (0.25 m<sup>2</sup>)

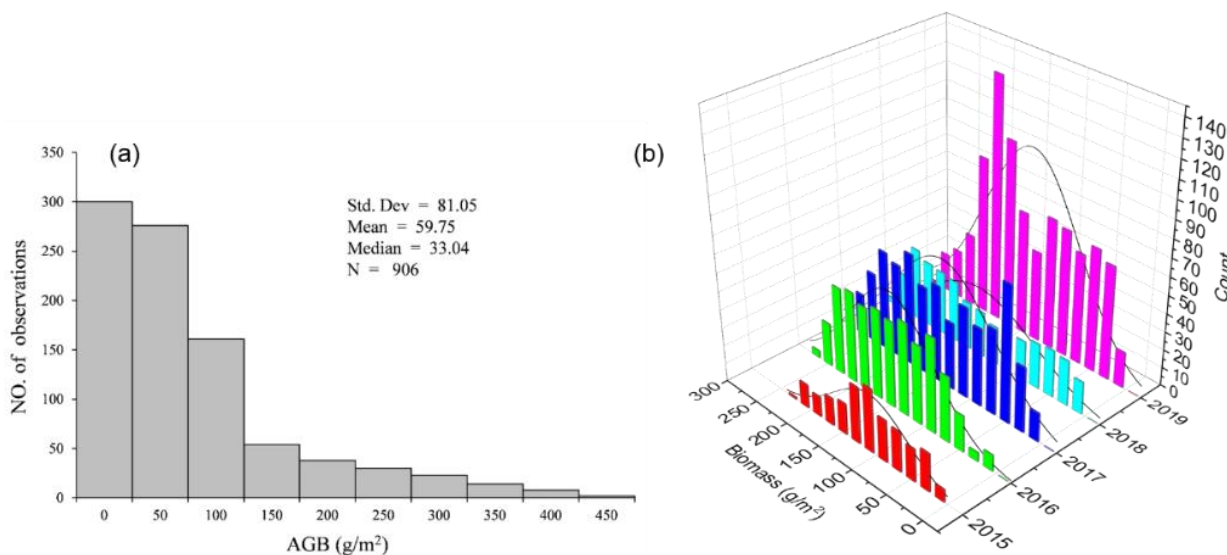
216 Since the spatial coverage of a 20m-high UAV photo (26 m×35 m) is much wider than a single 2m-high UAV photo, making  
217 it easier to match to the MODIS pixel scale. Hence, the 20m-high UAV photos containing the sample frames were chosen  
218 for constructing the quadrat-scale AGB estimation model. A total of 906 pairs of quadrat-scale UAV-field AGB observation  
219 data were collected, with good spatial representativeness (Figure 1 a, red dots). The observed AGB values ranged from 0 to  
220 450 g/m<sup>2</sup>, with mean and median values of 59.75 g/m<sup>2</sup> and 33.04 g/m<sup>2</sup>, respectively, most of which were less than 100 g/m<sup>2</sup>

221 (Figure 5a). The cropped 20-meter-high UAV image indices and the measured AGB values were used as the independent  
222 and dependent variables to build the RF model (Figure 2).

### 223 2.5.3 AGB calculation at the photo scale (~900 m<sup>2</sup>)

224 The steps for AGB estimation of the whole 20-meter-high UAV photo were as follows: 1) First, each UAV photo was  
225 divided into ~2,000 quadrat-sized small patches. 2) Second, the AGB of each small patch was calculated based on the  
226 quadrat-scale AGB estimation model. 3) Finally, the average of all small patches was calculated as the AGB of the whole  
227 photo. Based on the above steps, the AGB values of 37,487 images in GRID or RECTANGLE mode were calculated using  
228 more than 74 million AGB values of the quadrat scale (Table 1).

229



230

231 **Figure 5. Histograms of field-measured AGB values at quadrat scale (a) and UAV-estimated AGB values of different years at the**  
232 **photo scale (b).**

233

### 234 2.5.4 AGB RF model construction at MODIS pixel-scale (6,2500 m<sup>2</sup>)

235 The following steps were involved in constructing the AGB estimation model at the pixel scale. 1) Since the coverage of a  
236 GRID or RECTANGLE mode was similar to that of a MODIS pixel, the average of its 16 or 12 photos was taken as the  
237 AGB value of the corresponding pixel. From 2015-2019, a total of 2,602 UAV-estimated AGB samples were obtained at the  
238 pixel scale (Table 1). 2) The MODIS vegetation indices and other spatial metrics corresponding to each GRID or  
239 RECTANGLE mode were then extracted using the ArcGIS software. Here, the MODIS NDVI, EVI, and kNDVI indices  
240 closest to the sampling time were chosen to minimize the time difference between sampling and satellite overpass.3)

241 Subsequently, the UAV-estimated AGB values and the extracted spatial indices were used as dependent and independent  
242 variables to build the AGB estimated model at the pixel scale using the RF algorithm.

## 243 **2.6 Uncertainty analysis**

244 Since the actual AGB values of MODIS pixels cannot be directly obtained, vegetation indices were used to quantify the  
245 uncertainty of different AGB estimation methods. In other words, the higher the correlation between the estimated AGB and  
246 MODIS vegetation indices, the more accurate the estimation model was. The performance of the estimation model was  
247 evaluated through three aspects. In this study, we first compared the correlation between the MODIS vegetation indices and  
248 AGB values obtained by traditional sampling and UAV estimation methods. We also explored the uncertainties of UAV  
249 sampling coverage by randomly combining the number of photos in a MODIS pixel, and tested whether the estimated AGB  
250 was closer to the true value as the number increased. Furthermore, the AGB validation results from GRID or RECTANGLE  
251 at the pixel scale were compared to understand the uncertainties caused by different flight modes.

## 252 **2.7 Trend analysis of grassland AGB**

253 This study combined the Theil-Sen median trend analysis and Mann-Kendall test to analyze the temporal variation  
254 characteristics of grassland AGB of QTP (Jiang et al., 2015). Theil-Sen median trend analysis is a robust trend statistical  
255 method with high computational efficiency, insensitive to outliers (Hoaglin et al., 1983). The Mann-Kendall test is a  
256 nonparametric test for time series trends, which does not require the measurements to follow a normal distribution and is not  
257 affected by missing values and outliers. The Theil-Sen Median trend analysis and Mann-Kendall trend test have been widely  
258 used to analyze vegetation index, cover, and biomass (Gao et al., 2020; Jiang et al., 2015; Fensholt et al., 2009). The  
259 formulas for the Theil-Sen median trend analysis and the Mann-Kendall method are detailed in Jiang et al. (2015).

## 260 **3 Results**

### 261 **3.1 Independent variables selected for AGB modeling**

262 The independent variables for AGB estimation at the quadrat and pixel scales were presented in Table 2. A total of 36  
263 independent variables were selected at the quadrat scale, including 26 vegetation RGB indices, 6 histogram indices, and 4  
264 color space indices (Figure A2). At the pixel scale, five variables were selected, including NDVI, kNDVI, EVI, PREC, and  
265 DEM (Figure A3).

266  
267

268 **Table 2: Selected independent variables for the AGB modeling at quadrat and pixel scales. The full names of each variable at the**  
 269 **quadrat scale were listed in Table A3.**

Scale	Model	Number	Independent variables
Quadrat	RF <sub>Q</sub>	36	FVC, WI, GI, EXG, TGI, EXGR, VEG, GRATIO, COM, CIVE, RGBVI, EXR, GLA, GRRI, MVARI, MGRVI, GRVI, RGRI, GBRI, VARI, NDI, RRATIO, EXB, V, IPCA, INT, HOC_R_CORR, HOC_B_CHIS, HOC_R_CHIS, HOC_G_CHIS, HOC_G_CORR, HOC_B_CORR B, H, G, R,
Pixel	RF <sub>P</sub>	5	NDVI, kNDVI, EVI, DEM, PREC

270

### 271 3.2 Modeling and accuracy assessment

272 For the AGB estimation model at the quadrat scale, the results of 10-cross validations showed that there was a significant  
 273 linear relationship between the estimated and the measured values ( $R^2=0.73$ ,  $p<0.001$ , Table 3, Table A4). The student's t-  
 274 test was also used to assess whether there was a significant difference between the predicted AGB values and the measured  
 275 values at a confidence level of 95%. As shown in Table 4, there was no significant difference ( $p=0.51>0.05$ ) with an RMSE  
 276 of 32.94 g/m<sup>2</sup>. The scatter plot showed that the model predicted well when the measured biomass was less than 150g/m<sup>2</sup>, but  
 277 showed some underestimation when it was more than 200g/m<sup>2</sup> (Figure 6a). It may be because the number of samples more  
 278 than 200g/m<sup>2</sup> is relatively small, accounting for only 8.50% of all samples (Figure 5a). Although the sample size of UAVs  
 279 varied from year to year, most of the AGB values estimated from photos ranged from 0 to 300 g/m<sup>2</sup> (Figure 5b).

280

281 For the pixel-scale AGB estimation model, there was a strong linear relationship between the predicted AGB and UAV  
 282 estimates for 2015-2019 (Table A4). The fitting coefficient  $R^2$  was 0.85 for 2017-2019, and slightly lower for 2015-2016 at  
 283 0.63 and 0.77, respectively (Table 3, Figure 6b-f). The RMSE of the pixel-scale model ranged from 23.36 to 34.07 g/m<sup>2</sup>  
 284 (Table 3). In addition, we found no significant differences between the predicted and measured average AGB values except  
 285 for 2017 and 2018 (Table 4). While the average model projections for 2017 and 2018 were 14.72% and 13.78% lower than  
 286 the UAV estimates, they were within acceptable ranges. Therefore, the constructed pixel-scale AGB estimation model had  
 287 good performance and robustness in different years (Figure 6b~f).

288

289

290 **Table 3: Validation results of AGB models at quadrat and pixel scales**

Scale	Year	Training set		Validation set	
		R <sup>2</sup>	RMSE(g/m <sup>2</sup> )	R <sup>2</sup>	RMSE(g/m <sup>2</sup> )
Quadrat-scale	2019	0.94	20.18	0.73 ***	32.94
Pixel-scale	2019	0.96	10.68	0.85 ***	23.36
	2018	—	—	0.85 ***	24.83
	2017	—	—	0.85 ***	23.83
	2016	—	—	0.77 ***	31.28
	2015	—	—	0.63 ***	34.07

291 '\*\*\*' significant at p&lt;0.001

292

293

294 **Table 4: T-test results between the predicted and measured AGB values for the modes at the quadrat and pixel scales**

Validation model	Measured mean	Predicted mean	t	df	p-value
2019_Quadrat-scale	51.57	54.35	-0.66	939.35	0.51
2019_Pixel_scale	136.68	137.7461	-0.15	340.78	0.88
2018_Pixel_scale	152.49	131.48	4.01	723.81	6.63e-05
2017_Pixel_scale	141.42	120.60	5.48	1225.2	5.26e-08
2016_Pixel_scale	149.56	142.70	1.68	961.99	0.09413
2015_Pixel_scale	108.65	98.23	1.96	1225.2	0.05

295

296

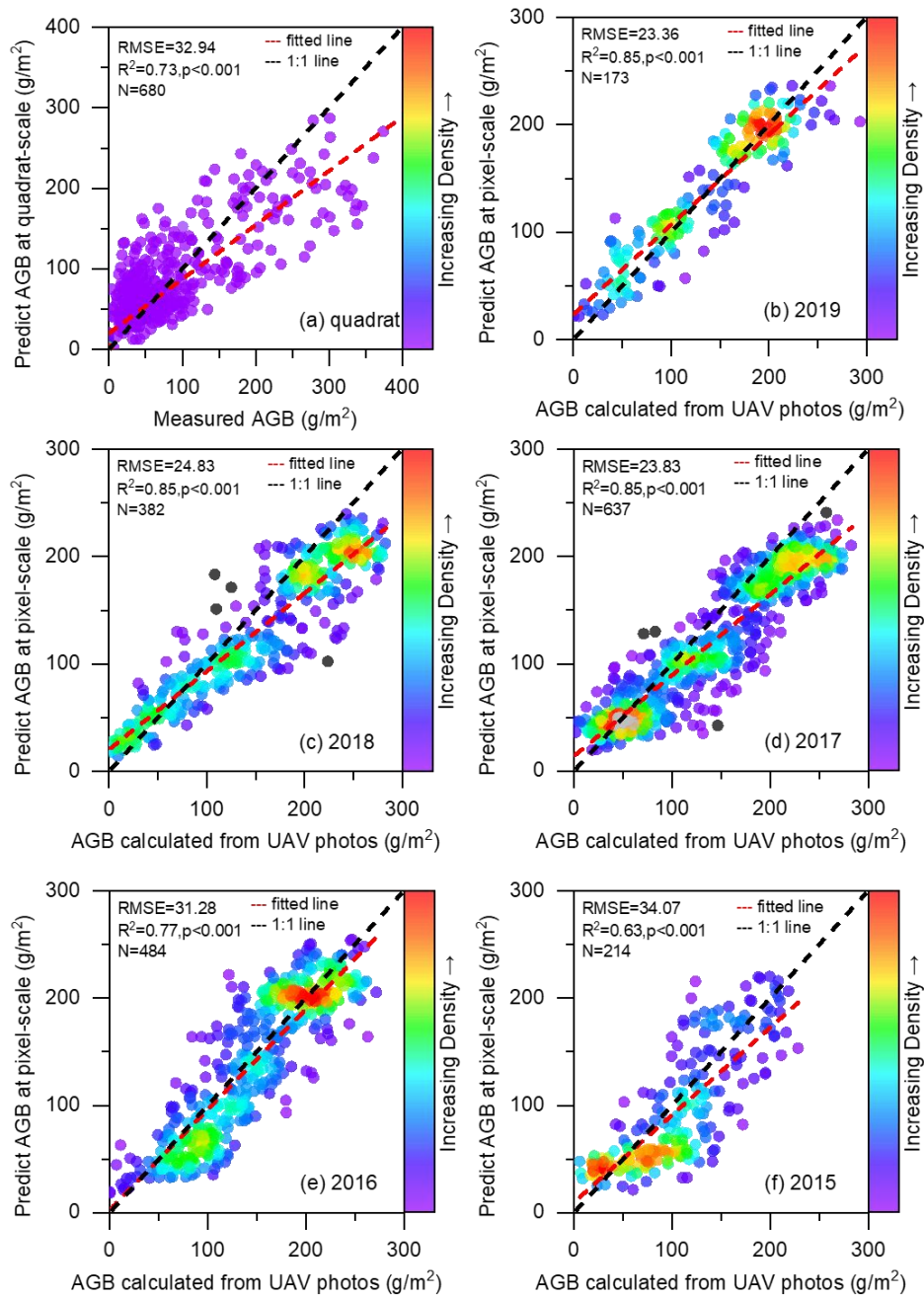
297 **3.3 Correlation analysis between AGB values and MODIS indices**

298 The correlations between the UAV-estimated AGB values and MODIS vegetation indices were much better than the  
299 traditional sampling method (Figure 7a). For example, the correlation between NDVI and traditionally measured AGB was  
300 only 0.53, much lower than that obtained from a single UAV image ( $r=0.74$ ). Moreover, the correlation between NDVI and  
301 UAV-estimated AGB increased with the number of UAV photos. It increased rapidly as the number increased from 1 to 4  
302 (from 0.74 to 0.86), then slowed down and stabilized (from 0.87 to 0.88). In addition, we compared the scatter plots and  
303 fitting lines between NDVI and different AGB estimation methods (Figure 7b-f). The results showed a weak linear  
304 relationship between the traditionally measured AGB and NDVI, with an R<sup>2</sup> of 0.29. With the UAV sampling method, the  
305 linear relationship was greatly improved and increased with the number of photographs. The fit coefficient R<sup>2</sup> increased from  
306 0.54 to 0.78, much higher than the traditional sampling method (Figure 7).

307

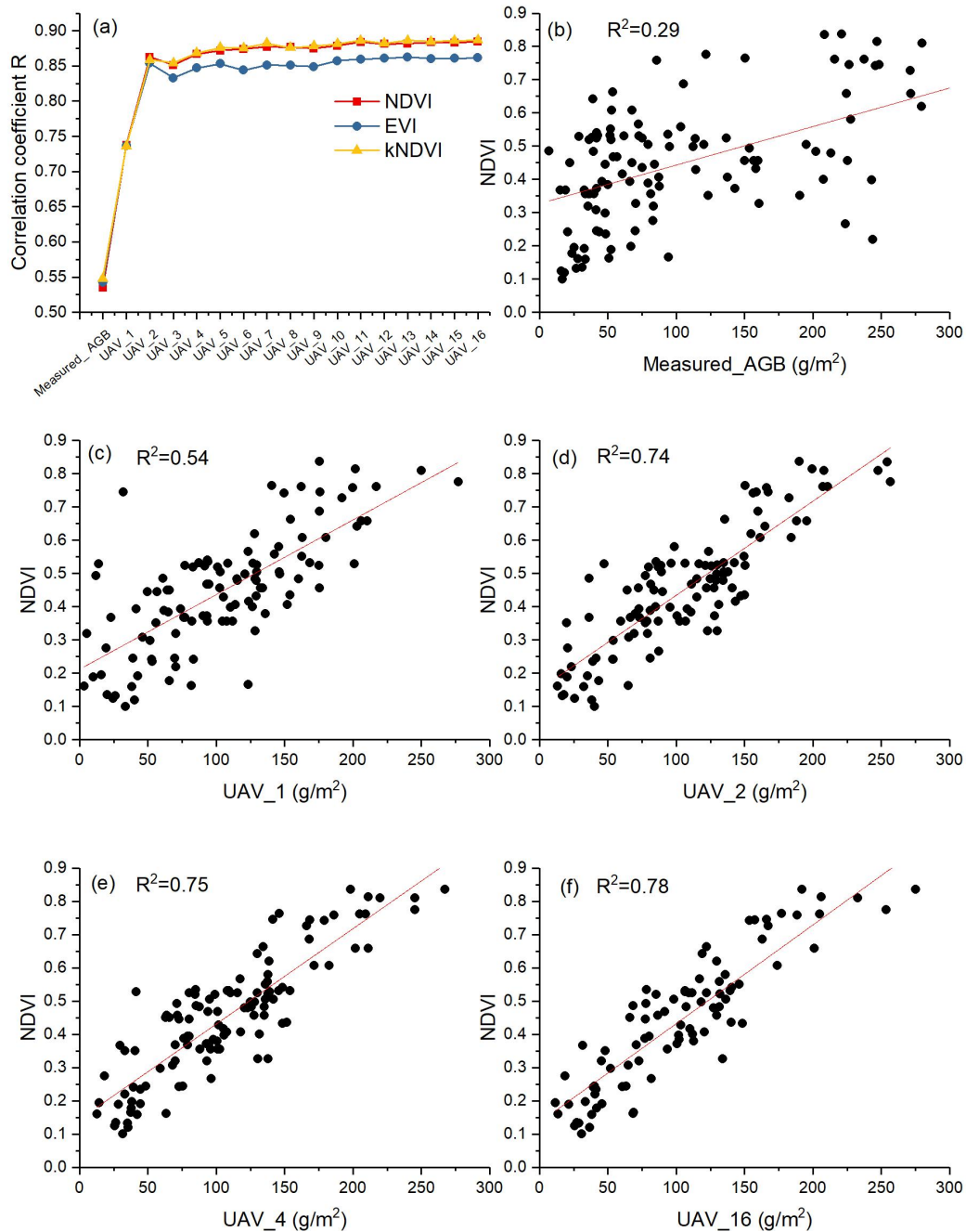
308

309



310  
 311  
 312  
 313

Figure 6. Validation results of the AGB estimation models at the quadrat (a) and MODIS pixel scale for 2015-2019 (b~f).



314  
 315 **Figure 7. Correlation between MODIS vegetation indices and different AGB estimation methods (a); scatter plots of NDVI with**  
 316 **different AGB estimation methods (b-f). UAV\_x, x represents the number of UAV photos used to estimate the average AGB at the**  
 317 **MODIS pixel scale. Here, x ranges from 1 to 16.**

318

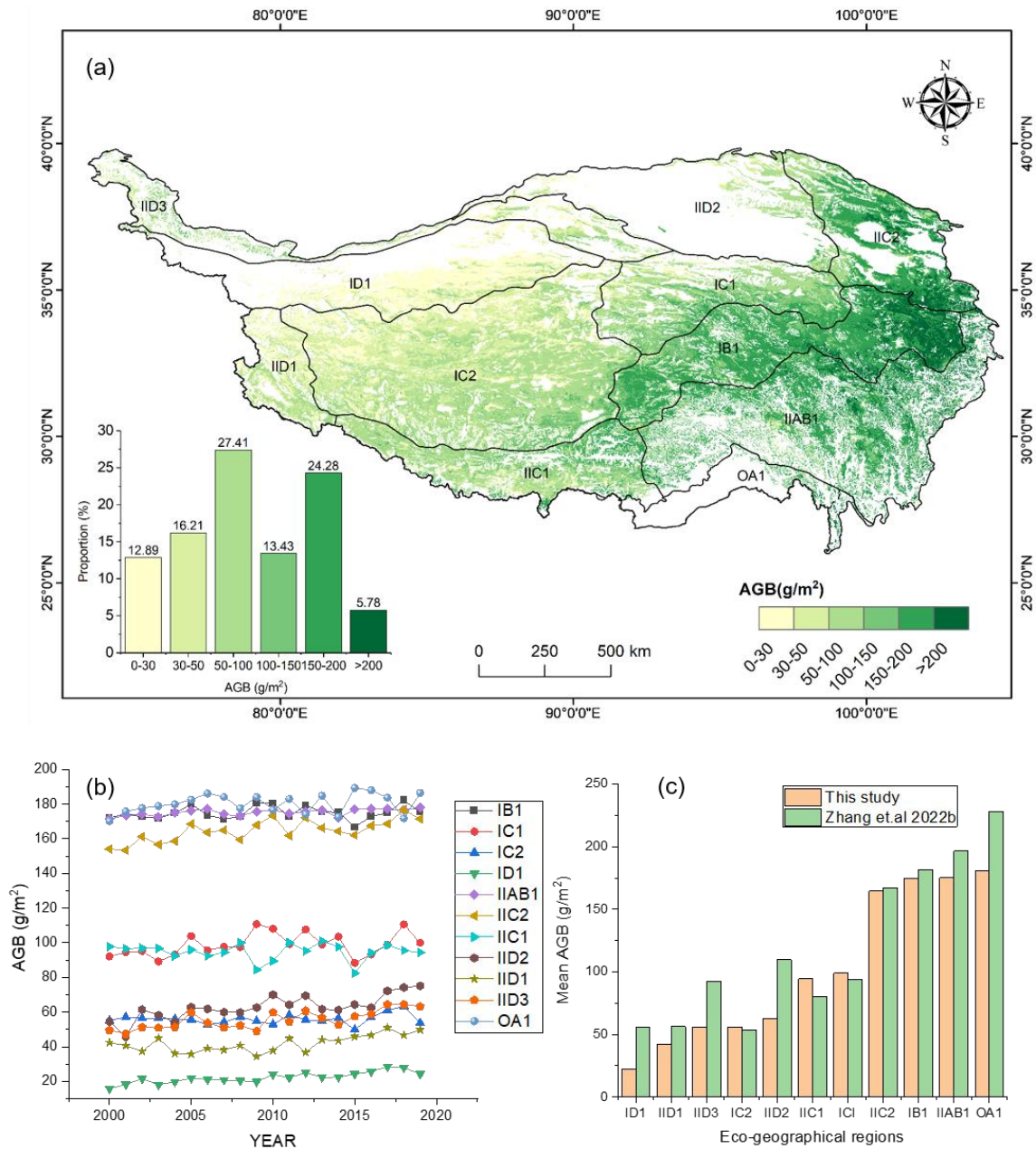


### 320 **3.4 Spatial distribution of grassland AGB**

321 The spatial distribution of the average grassland AGB on the QTP from 2000 to 2019 was calculated (Figure 8). The AGB  
322 gradually increased from west to east. As shown in Figure 8b, the average biomass of eastern OA1, IIAB, IB1, and IIC2 eco-  
323 geographical regions ranged from 150 to 190 g/m<sup>2</sup>, and the average AGB of IC1 and IIC1 ranged from 80 to 110 g/m<sup>2</sup>. The  
324 average AGB of IID2, IID3, IC2, and IID1 in the west was relatively low, ranging from 35 to 75 g/m<sup>2</sup>. The ID1 region was  
325 dominated by sparse grassland with the lowest average interannual AGB values, which fluctuated around 20 g/m<sup>2</sup> (Figure  
326 8b). The average AGB of QTP showed an insignificant increasing trend between 2000 and 2019, with an average growth  
327 rate of 0.22 gm<sup>-2</sup>a<sup>-1</sup> (Figure 9a). The overall mean AGB of the QTP was 103.6 g/m<sup>2</sup>, with 151.85 g/m<sup>2</sup>, 60.85 g/m<sup>2</sup>, and 28.91  
328 g/m<sup>2</sup> for alpine meadow, alpine steppe, and sparse grassland, respectively (Figure 9b). In addition, the temporal trend of  
329 grassland AGB in each pixel was analyzed. As shown in Figure 10, the IID3, ID1, IID2, and IIC2 eco-geographical regions  
330 of the northern QTP showed an increasing trend from 2000 to 2019, while the IC2, IB1, and IIC1 regions showed some  
331 degradation. Therefore, there was spatial heterogeneity in the temporal variation.

332

333

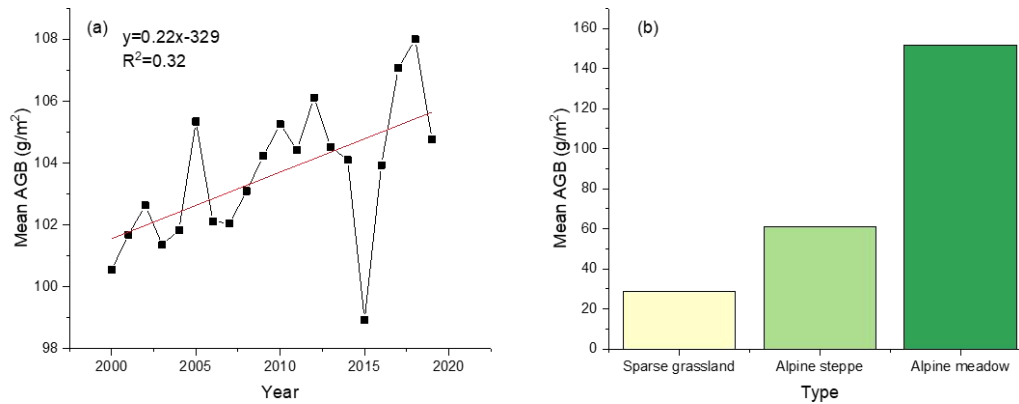


334

335

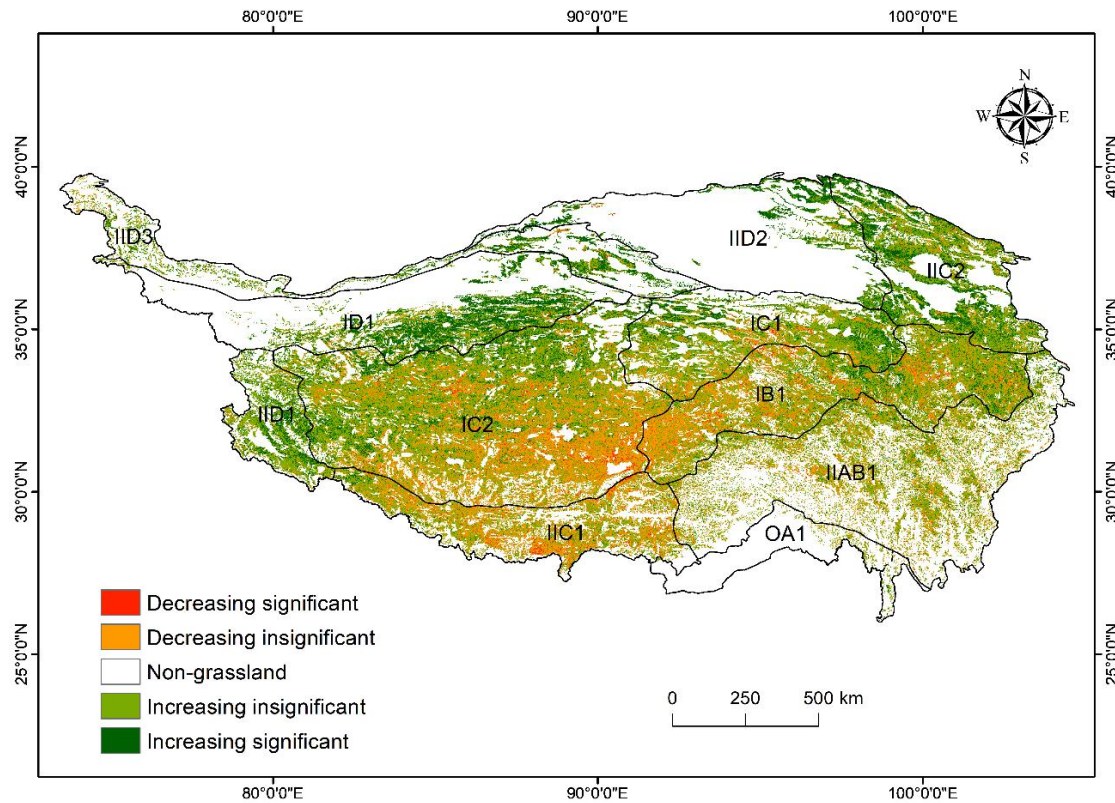
336 **Figure 8. (a) The spatial distribution of average grassland AGB on the QTP from 2000 to 2019. IID1, IID2, IID3, ID, IIC1, IIC2,**  
 337 **IC1, IB1 IAB1, and OA1 are the eco-geographical regions of the QTP(Zheng, 1996). The full names of each eco-geographical**  
 338 **region were listed in Table A5. (b) AGB values of each eco-geographical region from 2000 to 2019. (c) Comparison of multi-year**  
 339 **AGB averages in the different eco-geographical regions.**

340



341

342 **Figure 9. Variation trend of average grassland AGB on the QTP from 2000 to 2019 (a) and average AGB of different grassland**  
 343 **types (b).**



344

345 **Figure 10. Spatial trends of grassland AGB on the QTP from 2000 to 2019. IID1, IID2, IID3, ID, IC1, IC2, IB1, IAB1, and**  
 346 **OA1 are the eco-geographical regions of the QTP (Zheng, 1996). The full names of each eco-geographical region were listed in**  
 347 **Table A5.**

348

## 350 4. Discussion

### 351 4.1 Scale matching and its influence factor

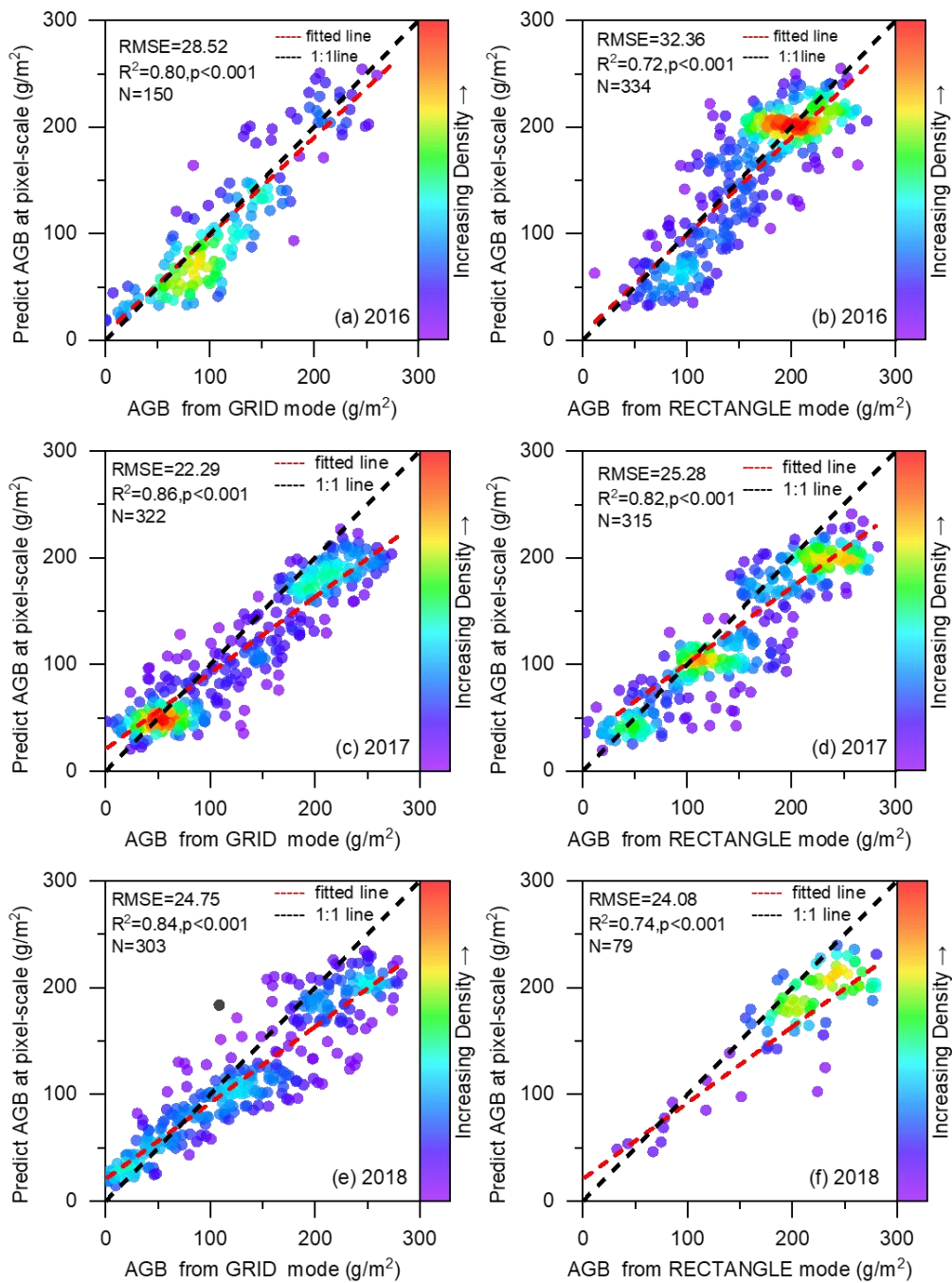
352 In previous studies, the AGB value of a satellite pixel was represented by the average value of 3-5 quadrat-scale samples, so  
353 there is a large spatial gap between the ground samples and the satellite pixels (Yang et al., 2017; Yang et al., 2009; Meng et  
354 al., 2020). The spatial gap between ground samples and satellite indices affects the accuracy of grassland AGB models. The  
355 smaller the spatial gap between the two, the higher the accuracy of the model (Morais et al., 2021). We addressed this issue  
356 using the UAVs as a bridge to reduce the spatial gap. Spatial scale matching of dependent and independent variables was  
357 achieved in estimating AGB values at different scales. First, at the quadrat scale, the independent variables were all derived  
358 from cropped 20-meter-high UAV images corresponding to the ground samples (Figure 3e). Then, the 20-meter-high UAV  
359 image was cropped into ~2000 quadrat-sized patches to ensure consistency with the quadrat-scale model, and the average of  
360 these patches was used as the final AGB at the photo scale. Finally, by averaging the AGB of 16 or 12 UAV photos within  
361 the MODIS pixel, the AGB value matching the MODIS pixel scale was calculated (Figure A1). With these three steps, we  
362 successfully upscaled the measured AGB from the traditional quadrat scale (0.5 m×0.5 m) to the photo scale (26 m×35 m)  
363 and MODIS pixel scale (250 m×250 m). Our results showed that the correlations between the UAV-estimated AGB values  
364 and the MODIS vegetation indices were higher than that of the traditional sampling method (Figure 7).

365

366 Furthermore, we found that the spatial coverage of the UAV sampling had an impact on the scale matching. Our results  
367 showed that the closer the spatial coverage of the UAV sampling was to the satellite pixel, the higher its correlation with  
368 MODIS spectral indices (Figure 7a). It was also confirmed by comparing the validation results of different flight modes. At  
369 the pixel scale, we found that the  $R^2$  between the model predictions and the AGB values estimated based on the GRID mode  
370 was better than that of RECTANGLE (Figure 11). The reason is that GRID mode can take 16 pictures within a MODIS pixel,  
371 while RECTANGLE mode only takes 12 pictures (Figure A1).

372

373 The above results confirmed that UAVs could serve as a bridge to effectively reduce the spatial gap between traditional  
374 samples and satellite data.



375

376 **Figure 11. Comparison of validation results for the GRID (a,c,e) and RECTANGLE (b,d,f) modes in 2016-2018.**

## 377 **4.2 Importance of the addition of non-vegetation samples**

378 Compared with traditional sampling, UAV sampling has the advantage of wide spatial coverage (0.5 m×0.5 m vs. 35 m×26  
379 m). Thus, the UAV image could capture vegetation and non-vegetation background information, such as roads, water, soil,  
380 gravel, riverbed, etc. (Figure A4). Adding non-vegetation samples could improve the accuracy of AGB estimation at the  
381 photo scale, especially for low-cover areas, to avoid overestimation. It was also true for the pixel-scale AGB estimation  
382 model. However, the traditional sampling method gave less consideration to the non-vegetation areas. The sample plots were  
383 mainly set in areas with homogeneous spatial distribution, and rarely in areas with spatial heterogeneity. This shortcoming  
384 may limit the accuracy of AGB estimation due to the high spatial heterogeneity of the QTP. Fortunately, the UAV sampling  
385 method can avoid this drawback. It can objectively record surface information and reduce the influence of manual plot  
386 selection on AGB estimation.

## 387 **4.3 Comparison of the estimated AGB with previous studies**

388 We compared our results with previous studies at the quadrat, pixel, and regional scales.

389

390 At the quadrat scale, consistent with our previous study, we further confirmed that the UAV RGB images could be used to  
391 estimate grassland AGB (Zhang et al., 2022a; Zhang et al., 2018). Similar to the 2-meter-high UAV image, the indices from  
392 the 20-meter-high UAV image could be used to estimate the grassland AGB at the quadrat scale ( $R^2=0.73$ ,  $RMSE=44.23$   
393  $g/m^2$ , Figure 6a). Compared with the 2-meter-high UAV image, the 20-meter-high UAV image is more suitable for  
394 matching the MODIS pixel due to its wider spatial coverage (26 m ×35 m).

395

396 At the pixel scale, compared with other studies, this paper achieved the spatial scale matching of independent and dependent  
397 variables during the modeling. In previous studies (Yang et al., 2009; Yang et al., 2017; Meng et al., 2020), they  
398 constructed the models from the measured AGB values at the quadrat-scale and the spectral indices of the satellites without  
399 considering the spatial scale difference. It partly explained why the  $R^2$  of the AGB linear model constructed by Yang et al.  
400 was only 0.4 (Yang et al., 2009). Our results confirmed that the  $R^2$  of the linear model could be increased from 0.29 to 0.78  
401 after reducing the spatial gap between measured AGB and NDVI (Figure 7). In addition, thanks to the rapid sampling of  
402 UAV AGB, a total of 2,602 samples matching the pixel scale were collected during 2015-2019. It allowed us to perform  
403 cross-year validation to assess the robustness of the model over time, which has rarely been performed in previous studies.  
404 Our results showed similar validation results for 2017-2019 ( $R^2=0.85$ ,  $p<0.001$ ) despite different sample sizes and spatial  
405 distributions (Figure 1, Table 1). But in 2015-2016,  $R^2$  was relatively low, at 0.63 and 0.77, respectively (Table 3, Figure 6).  
406 The reason was that during 2015-2016, some photos with abnormal white balance were obtained due to improper settings,  
407 which reduced the estimation accuracy (Figure A5). The validation results showed that the pixel-scale AGB estimation  
408 model had good robustness in different regions and times when the photo quality was acceptable.

409 **Table 5: Comparison of AGB estimation results of different studies on the QTP**

Mean AGB (g/m <sup>2</sup> )	Alpine steppe (g/m <sup>2</sup> )	Alpine meadow (g/m <sup>2</sup> )	Study period	Approach	Input parameter	References
68.8	50.1	90.8	2001-2004	Linear regression	EVI	(Yang et al., 2009)
	22.4	42.37	2000-2012	Linear regression	NDVI	(Liu et al., 2017)
120.73	—	—	1980–2014	Exponential regression	NDVI	(Jiao et al., 2017)
78.4			1982-2010	RF	NDVI, climate	(Xia et al., 2018)
77.12	76.43	154.72	2000-2014	RF	NDVI, EVI, climate, terrain	(Zeng et al., 2019)
59.63	42.75	77.56	2000-2017	RF	NDVI, climate	(Gao et al., 2020)
102.4	—	—	2000-2020	RF	climate, soil, and terrain	(Zhang et al., 2022b)
70.00	—	—	1960–2002	Century	climate and soil data	(Zhang et al., 2007)
119.78	—	—	2002–2004	Orchidee	climate, soil and LAI data	(Tan et al., 2010)
103.6	60.85	151.85	2000-2019	RF	MODIS	this study

410

411 At the regional scale, consistent with previous results, we found an overall increase in AGB over the QTP from 2001 to 2019,  
412 albeit with fluctuations (Zeng et al., 2019; Gao et al., 2020). The annual average AGB of grassland was 103.6 g/m<sup>2</sup>, which  
413 was closest to Zhang et al.(Zhang et al., 2022b) and within the range of the previous estimates ( 59.63-120.73 g/m<sup>2</sup> ) (Table  
414 5). The mean AGB varied among different grassland types, with 151.85 g/m<sup>2</sup> for the alpine meadow and 60.85 g/m<sup>2</sup> for the  
415 alpine steppe. Our estimation results were similar to those of Zeng et al. (Zeng et al., 2019), but the overall average AGB  
416 was higher than their estimate of 77.12 g/m<sup>2</sup>. The spatial distribution of AGB was consistent with previous studies, showing  
417 a west-to-east increasing trend (Zhang et al., 2022b; Xia et al., 2018). Specifically, the average AGB of OA1, IIAB, IB1, and  
418 IIC2 eco-geographical regions in the east was significantly higher than that of IID2, IID3, IC2, IID1, and ID1 regions in the  
419 west (Figure 8). In general, the average AGB estimates for each eco-geographical region in this paper were not much  
420 different from those of Zhang et al. (2022b). Among them, our average AGB estimates for ID1, IID1, IID3, and IID2 regions  
421 were slightly lower, but our values were closer to the measured values of these regions (Figure 8c). The reason may be that  
422 they calculated the potential AGB, while we calculated the actual AGB, so our estimate was relatively low. In terms of  
423 spatial and temporal trends, the data results showed that the eco-geographical regions in the northern part of the QTP  
424 demonstrated an increasing trend (IID3, ID1, IID2, and IIC2), while the IC2, IIC1, and IB1 regions exhibited significant or  
425 non-significant decrease, which was consistent with the results of others (Gao et al., 2020; Liu et al., 2017).

426

427 The difference between our estimated grassland AGB and previous studies might be due to differences in data sources and  
428 modeling methods. Firstly, the sample size and spatial distribution of ground samples were different. The number of ground  
429 samples is the most important variable affecting the accuracy of the grassland AGB estimation model (Morais et al., 2021).

430 Unlike previous studies, we collected ground validation data by combining the traditional sampling method and UAVs. The  
431 newly proposed method could overcome the shortcomings of traditional samplings (time-consuming and labor-intensive). It  
432 no longer takes years to obtain spatially representative, large-scale ground validation data (Yang et al., 2017). With UAV  
433 sampling, ground observations matching the satellite pixel scale can be obtained in only 15-20 minutes, which is difficult to  
434 achieve in traditional surveys. Our new sampling method not only accelerates the sampling speed and increases the sample  
435 size, but also improves the spatial match between ground samples and satellite pixels. As a result, our ground validation data  
436 is superior to previous studies in terms of quantity and spatial match to the satellite data. Secondly, the input parameters of  
437 AGB estimation models were different. Some scholars used only a single vegetation index (NDVI or EVI), while others  
438 combined the vegetation index with meteorological, soil, and terrain indices to construct the AGB estimation models (Table  
439 5). In this study, NDVI, kNDVI, EVI, DEM, and PREC were used as the final predictor variables to construct the AGB  
440 estimation model at the pixel scale (Table 2). Thirdly, modeling methods might also affect the simulation results. As shown  
441 in Table 5, the overall AGB averages of the QTP estimated based on different methods (such as linear or nonlinear  
442 regression, machine learning, and ecological process model methods) varied considerably. Yang et al.(2017) found that the  
443 model performance of ANN was much better than the linear regression model when using the same dataset to estimate  
444 grassland AGB in the Three-River Headwaters Region of China. Jia et al.(2016) reported that the model forms could bring  
445 13% uncertainty to the AGB estimation. Wang et al. compared the RF with the support vector regression (SVR) machine  
446 learning algorithm and found that the RF yielded the best performance in grassland biomass estimation (Wang et al., 2017).  
447

#### 448 **4.4 Limitations and further work**

449 We acknowledge that there are some shortcomings in this study. 1) The predicted values of the quadrat-scale model were  
450 underestimated when the measured biomass values were greater than 250 g/m<sup>2</sup> (Figure 6). One reason may be that the  
451 number of samples greater than 250 g/m<sup>2</sup> was relatively small, accounting for only 5.18 % of all samples. Another reason  
452 may be that for high biomass grasslands, a single UAV RGB photo can only reflect information such as vegetation cover and  
453 greenness, but not height information. This feature is very unfavorable for estimating AGB in grassland areas with high  
454 vegetation coverage and height. Studies have shown that adding vegetation height information can help improve the  
455 estimation accuracy of grassland AGB (Zhang et al., 2022a; Lussem et al., 2019; Viljanen et al., 2018). In future work, an  
456 affordable DJI Zensil L1 Lidar UAV will be introduced to invert the height of the grassland. 2) At the pixel scale, limited by  
457 the estimation accuracy of AGB from UAV, there was also some underestimation in the high biomass area. Although the  
458 MODIS index closest to the sampling time was chosen for the construction/validation of the AGB estimation model, there  
459 was still a time difference between the measured samples and the MODIS indices, which might lead to estimation errors. In  
460 addition, the NDVI saturation problem was not considered in this study, which might affect the AGB estimation accuracy of  
461 QTP (Tucker, 1979a; Gao et al., 2000; Mutanga and Skidmore, 2004; Tucker, 1979b). In the next step, we will continue to  
462 collect samples with high biomass and try to correct the NDVI saturation problem to optimize the simulation accuracy of the



463 data set. 3) During 2015-2016, our study had just started, and the appropriate camera parameters were still being explored.  
464 As a result, some photos with abnormal white balance were obtained, reducing the accuracy of AGB estimation at the photo  
465 scale (Figure A5). 4) We collected grassland AGB only during the peak growing season, and the applicability of the  
466 proposed method to other growing seasons needs further study. 5) During the modeling process, due to the limited  
467 positioning accuracy, only the center points of the flight path were used to find the corresponding MODIS pixels. Moreover,  
468 although the UAV images in GRID or RECTANGLE mode could cover most areas of a MODIS pixel, full pixel coverage  
469 was still not achieved. Therefore, we will gradually upscale to MODIS pixels by combining UAVs with Sentinel-2 or  
470 Landsat images.  
471

## 472 **5. Data availability**

473 The dataset is available from the National Tibetan Plateau/Third Pole Environment Data Center  
474 (<https://doi.org/10.11888/Terre.tpd.c.272587>). The dataset contains 20 years of AGB spatial data of the QTP with a resolution  
475 of 250 m and is stored in TIFF format. The name of the file is "AGB\_yyyy.tif", where yyyy represents the year. For example,  
476 AGB\_2000.tif represents this TIFF file describing the alpine grassland AGB condition of QTP in 2000. The data can be  
477 readily imported into standard geographical information system software (e.g., ArcGIS) or accessed programmatically (e.g.,  
478 MATLAB, Python).

## 479 **6. Conclusion**

480 In this study, a new AGB dataset for alpine grasslands on the QTP was calculated based on traditional ground sampling,  
481 UAV photography, and MODIS imagery. The uniqueness of this dataset is the use of UAVs as a spatial scale-matching  
482 bridge between traditional samples and satellite pixels. The study confirmed that the UAV images could be used for AGB  
483 estimation at the quadrat /pixel scale, with  $R^2$  of 0.73/0.83 and RMSE of 44.23/34.13 g/m<sup>2</sup>, respectively. At the pixel scale,  
484 the correlation between AGB estimated by UAV and MODIS vegetation index was higher than that of the traditional  
485 sampling method (0.88 vs. 0.53). Moreover, the spatial scale matching of the dependent and the independent variables was  
486 achieved during the modeling. In addition, we performed a cross-year validation of the pixel-scale AGB estimation model to  
487 confirm the robustness of the model and the accuracy of this dataset. The availability of the new dataset is helpful in many  
488 applications. First, this dataset provides reliable regional data for estimating grassland productivity, carbon storage,  
489 ecological carrying capacity, and ecological service functions (such as feed for grazing livestock) of the QTP. Second, the  
490 dataset can be used to understand the mechanisms of environmental processes, such as hydrological cycle processes, soil  
491 erosion and degradation, and carbon cycle processes in the QTP. In addition, this dataset can be used as input or validation  
492 parameters for various ecological models to understand the response mechanism of the QTP to global climate change.

493 **7. Author contributions**

494 HZ contributed to the study conceptualization, methodology, funding acquisition, and the original draft of the manuscript.  
495 ZT, BW, and HK contributed to resources and formal analysis. QY and YS contributed to data collection and manuscript  
496 review. BM, ML, and JC contributed to the methodology and reviewed the manuscript. YL and JZ participated in reviewing  
497 and editing the manuscript. SN contributed to the data collection and review of the manuscript. SY contributed to the study  
498 conceptualization, funding acquisition, and manuscript review. All authors have read and approved the manuscript.

499 **8. Competing interests**

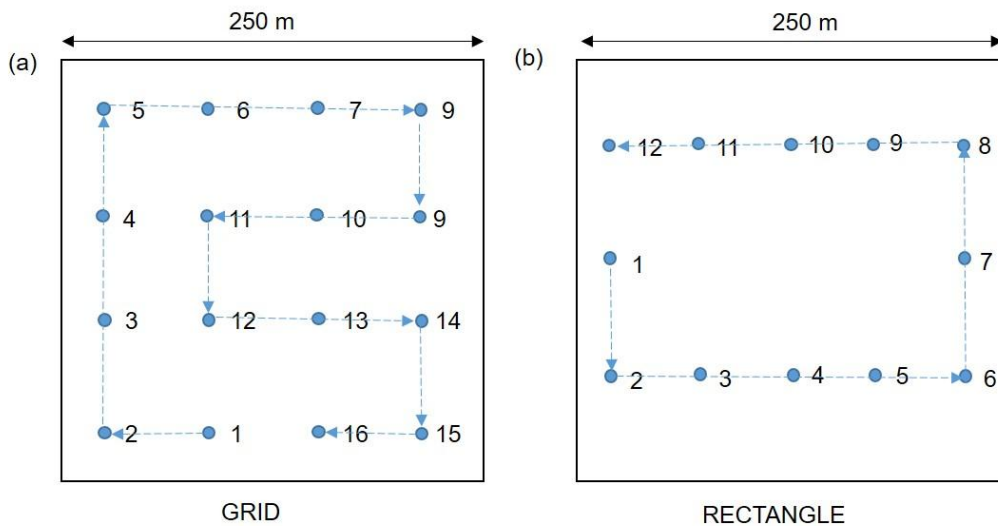
500 The authors declare that they have no conflict of interest.

501 **9. Acknowledgements**

502 We would like to express our gratitude to the other students and staff who participated in the field investigation.

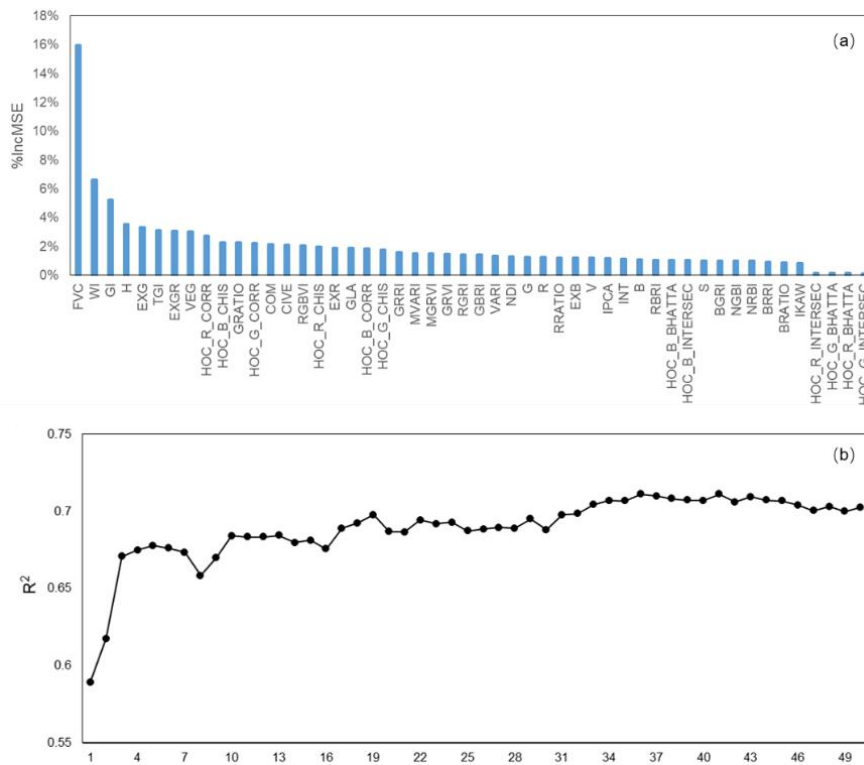
503 **10. Financial support**

504 This research was supported by the National Natural Science Foundation of China [grant nos: 41801023], the National Key  
505 R&D Program of China [grant nos: 2017YFA0604801], and the National Natural Science Foundation of China [grant nos:  
506 41801102].



508

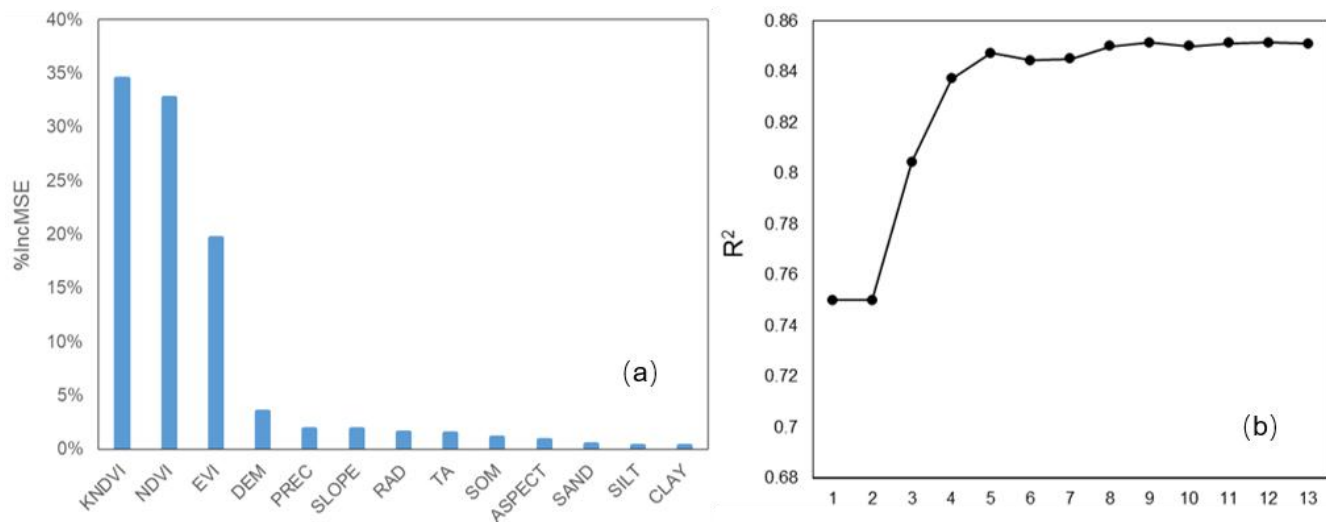
509 Figure A1. Waypoints for GRID (a) and RECTANGLE (b) flight modes.



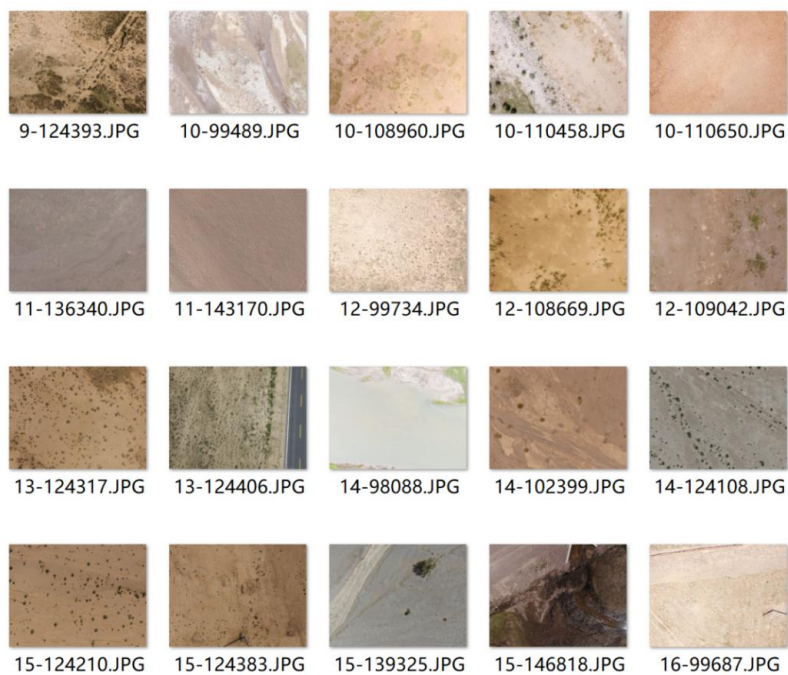
510

511 Figure A2. The importance values for each independent variable (a) and the  $R^2$  results of the different number of input variables

512 at the quadrat scale.

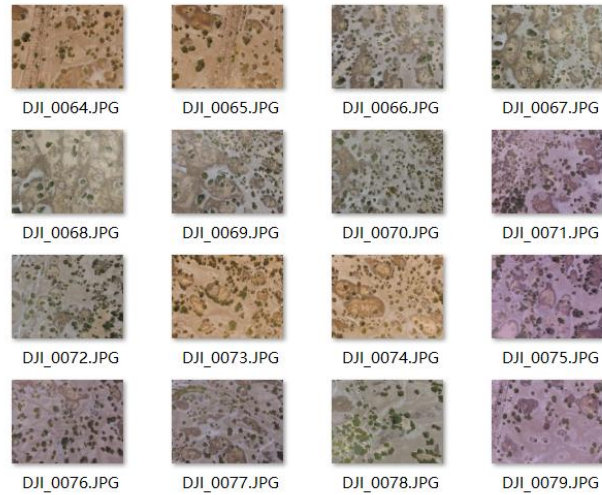


514

515 **Figure A3. The importance values for each independent variable (a) and the  $R^2$  results of the different number of input variables**516 **at the pixel scale.**

517

518 **Figure A4. Examples of 20-meter-high UAV images with different non-vegetation background information.**




519  
520 **Figure A5. An example of a set of GIRD photos with abnormal white balance in 2015.**

521  
522 **Table A1. Combined grassland types**

New grassland type	Original grassland type
Alpine meadow	Alpine meadow, Lowland meadow, Montane meadow,
Alpine steppe	Temperate steppe, Alpine steppe, Alpine meadow steppe
Spare grassland	Temperate steppe desert, Alpine desert

523  
524 **Table A2. Features of DJI Phantom 3 Pro**

	Features	Description
 DJI Phantom 3 Pro	Sensor	1/23-inch; Effective-pixel: 12-megapixel
	Filed of view	FOV 94° 20 mm
	Aperture	f/2.8
	Shooting speed	Electronic shutter: 8-1/8000 s
	Photo size	4000×3000
	Flight time	~25 min
	Image format	JPEG
	Hovering accuracy	±0.5 m vertically; ±1.5 m horizontally
	Weight	1280 g

525  
526

527 **Table A3: Details of the independent variables for quadrat-scale AGB estimation**

Acronym	Index name	Formula	Reference
GRVI	Green Red Vegetation Index	$(G-R)/(G+R)$	(Tucker, 1979a)
EXG	Excess Green Vegetation Index	$2G-R-B$	(Woebbecke et al., 1995)
GLA	Green leaf area	$(2G-R-B)/(2G+R+B)$	(Louhaichi et al.)
MGRVI	Modified Green Blue Vegetation Index	$(G2-R2)/(G2+R2)$	(Bendig et al., 2015)
RGBVI	Red Green Blue Vegetation Index	$(G2-B^*R)/(G2+B^*R)$	(Bendig et al., 2015)
EXB	Excess Blue Vegetation Index	$(1.4*B-G)/(G+R+B)$	(Maimaitijiang et al., 2019)
NDI	Normalized difference index	$(R-G)/(R+G)$	(Woebbecke et al., 1993)
EXR	Excess Red Vegetation Index	$1.4*R-B$	(Meyer and Neto, 2008)
EXGR	Excess Green minus Excess Red index	$ExG-ExR$	(Meyer and Neto, 2008)
RRATIO	Red Ratio	$R/(R+B+G)$	(Woebbecke et al., 1995)
BRATIO	Blue Ratio	$B/(R+B+G)$	(Woebbecke et al., 1995)
GRATIO	Green Ratio	$G/(R+B+G)$	(Woebbecke et al., 1995)
VARI	Visible Atmospherically Resistance Index	$(G-R)/(G+R-B)$	(Gitelson et al., 2002)
NRBI	Normalized Red Blue Index	$(R-B)/(R+B)$	(Michez et al., 2016)
NGBI	Normalized Green Blue Index	$(G-B)/(G+B)$	(Michez et al., 2016)
VEG	Vegetative index	$G/(RaB(1-a))$ , where $a=0.667$	(Hague et al., 2006)
WI	Woebbecke Index	$(G-B)/(R-G)$	(Woebbecke et al., 1995)
CIVE	Color Index of Vegetation	$0.441R$ $0.881G+0.385B+18.78745$	– (Kataoka et al., 2003)
COM	Combination Vegetative index	$0.25ExG+0.3ExGR+0.33CIVE$ $+0.12VEG$	(Guijarro et al., 2011)
TGI	Triangular Greenness Index	$G-0.39R-0.61B$	(Hunt et al., 2014; Michez et al., 2018)
RGBVI	Red Green Blue Vegetation Index	$(G2-B^*R)/(G2+B^*R)$	(Bendig et al., 2015)
GRR	Green Red Ratio Index	$G/R$	(Maimaitijiang et al., 2019)
GBRI	Green Blue Ratio Index	$G/B$	(Maimaitijiang et al., 2019)
RBRI	Red Blue Ratio Index	$R/B$	(Maimaitijiang et al., 2019)
BRRI	Blue Red Ratio Index	$B/R$	(Jibo et al., 2018)
BGRI	Blue Green Ratio Index	$B/G$	(Jibo et al., 2018)
RGRI	Red Green Ratio Index	$R/G$	(Jibo et al., 2018)
INT	Color Intensity Index	$(R+B+G)/3$	(Ahmad and Reid, 1996)
MVARI	Modified VARI	$(G-B)/(G+R-B)$	(Cen et al., 2019)
IPCA	Principal Component Analysis Index	$0.994 \times  R-B  + 0.961 \times  G-B  + 0.914 \times  G-R $	(Saberioon et al., 2014)

528

529

530

531 Table A3: Details of the independent variables for quadrat-scale AGB estimation (continued)

Acronym	Index name	Formula	Reference
R	An average value of R channel of the quadrat-scale UAV image		
G	An average value of G channel of the quadrat-scale UAV image		
B	An average value of B channel of the quadrat-scale UAV image		
H	An average value of H channel of the quadrat-scale image in HSV color space		
S	An average value of S channel of the quadrat-scale image in HSV color space		
V	An average value of V channel of the quadrat-scale image in HSV color space		
FVC	Fractional Vegetation Cover		
EGI	Extra Green Index	$EGI=2G-R-B$	
GI	Green Index	$GI=9 \times (H \times 3.14159 / 180) + 3 \times S + V$	(Zhang et al., 2022a)
HOC <sub><i>i</i></sub> ORR <sub>C</sub>	The histogram correlation coefficient between the <i>i</i> band and the black reference histogram, where the <i>i</i> represents the three bands of RGB	$corr = \frac{\sum_l (H_1(I) - \bar{H}_1)(H_2(I) - \bar{H}_2)}{\sqrt{\sum_l (H_1(I) - \bar{H}_1)^2 \sum_l (H_2(I) - \bar{H}_2)^2}}$	
HOC <sub><i>i</i></sub> INTERSE C	The histogram intersection coefficient between the <i>i</i> band and the black reference histogram, where the <i>i</i> represents the three bands of RGB	$intersec = \sum_l \min(H_1(I), H_2(I))$	
HOC <sub><i>i</i></sub> BHATTA	The histogram Bhattacharyya distance coefficient between the <i>i</i> band and the black reference histogram, where the <i>i</i> represents the three bands of RGB	$bhatta = \sum_l \min(H_1(I), H_2(I))$	
HOC <sub><i>i</i></sub> HIS	The histogram correlation coefficient between the <i>i</i> band and the black reference histogram, where the <i>i</i> represents the three bands of RGB.	$chis = \sum_l \frac{(H_1(I) - H_2(I))^2}{H_1(I)}$	

532

533 **Table A4: Regression analysis for AGB estimation models at quadrat and pixel scales**

<b>Model name</b>	<b>Coefficient</b>	<b>Value</b>	<b>Standard Error</b>	<b>t-Value</b>	<b>p-value</b>
2019_Quadrat-scale	Slope	0.67	0.016	42.58	9.05e-194
	Intercept	20.10	1.49	13.59	5.96e-37
2019_Pixel_scale	Slope	0.84	0.03	31.59	2.75e-73
	Intercept	23.20	4.04	5.74	4.24e-8
2018_Pixel_scale	Slope	0.73	0.02	45.81	8.28e-157
	Intercept	20.43	2.74	7.46	6.01e-13
2017_Pixel_scale	Slope	0.75	0.01	59.13	1.98e-260
	Intercept	13.89	2.04	6.82	2.19e-11
2016_Pixel_scale	Slope	0.94	0.02	40.45	4.69e-157
	Intercept	2.48	3.75	0.66	0.03
2015_Pixel_scale	Slope	0.82	0.04	18.88	2.59e-47
	Intercept	9.50	5.25	1.81	0.04

534

535 **Table A5: List of abbreviations of eco-geographical regions and the mean AGB of the QTP**

<b>Abbreviation</b>	<b>Full name</b>
IB1	Golog-Nagqu high-cold shrub-meadow zone
IIAB1	Western Sichuan-eastern Tibet montane coniferous forest zone
IC1	Southern Qinghai high-cold meadow steppe zone
IC2	Qiangtang high-cold steppe zone
ID1	Kunlun high-cold desert zone
IIC1	Southern Tibet montane shrub-steppe zone
IIC2	Eastern Qinghai-Qilian montane steppe zone
IID1	Nagri montane desert-steppe and desert zone
IID2	Qaidam montane desert zone
IID3	Northern slopes of Kunlun montane desert zone
OA1	Southern slopes of Himalaya montane evergreen broad-leaved forest zone

536

537 **References**

- 538 Ahmad, I. S. and Reid, J. F.: Evaluation of Colour Representations for Maize Images, *Journal of Agricultural Engineering Research*, 63,  
539 185-195, doi:10.1006/jaer.1996.0020 1996.4
- 540 Bendig, J., Yu, K., Aasen, H., Bolten, A., Bennertz, S., Broscheit, J., Gnyp, M. L., and Bareth, G.: Combining UAV-based plant height  
541 from crop surface models, visible, and near infrared vegetation indices for biomass monitoring in barley, *International Journal of Applied*  
542 *Earth Observation & Geoinformation*, 39, 79-87, doi:10.1016/j.jag.2015.02.012, 2015.4
- 543 Bian, L. and Walsh, S. J.: Scale dependencies of vegetation and topography in a mountainous environment of Montana, *The Professional*  
544 *Geographer*, 45, 1-11, doi:10.1111/j.0033-0124.1993.00001.x, 1993.4



545 Breiman, L.: Random forests, *Machine learning*, 45, 5-32, doi:10.1023/A:1010933404324, 2001.4

546 Camps-Valls, G., Campos-Taberner, M., Moreno-Martinez, A., Walthers, S., Duveiller, G., Cescatti, A., Mahecha, M. D., Munoz-Mari, J.,  
547 Garcia-Haro, F. J., Guanter, L., Jung, M., Gamon, J. A., Reichstein, M., and Running, S. W.: A unified vegetation index for quantifying  
548 the terrestrial biosphere, *Sci Adv*, 7, eabc7447, doi:10.1126/sciadv.abc7447, 2021.4

549 Cannavacciuolo, M., Bellido, A., Cluzeau, D., Gascuel, C., and Trehen, P.: A geostatistical approach to the study of earthworm  
550 distribution in grassland, *Applied Soil Ecology*, 9, 345-349, doi:10.1016/S0929-1393(98)00087-0, 1998.4

551 Cen, H. Y., Wan, L., Zhu, J. P., Li, Y. J., Li, X. R., Zhu, Y. M., Weng, H. Y., Wu, W. K., Yin, W. X., Xu, C., Bao, Y. D., Feng, L., Shou, J.  
552 Y., and He, Y.: Dynamic monitoring of biomass of rice under different nitrogen treatments using a lightweight UAV with dual image-  
553 frame snapshot cameras, *Plant Methods*, 15, doi:10.1186/s13007-019-0418-8, 2019.4

554 Chen, J., Yi, S., Qin, Y., and Wang, X.: Improving estimates of fractional vegetation cover based on UAV in alpine grassland on the  
555 Qinghai-Tibetan Plateau, *International Journal of Remote Sensing*, 37, 1922-1936, doi:10.1080/01431161.2016.1165884, 2016.4

556 Cheng, X., An, S., Chen, J., Li, B., Liu, Y., and Liu, S.: Spatial relationships among species, above-ground biomass, N, and P in degraded  
557 grasslands in Ordos Plateau, northwestern China, *Journal of Arid Environments*, 68, 652-667, doi:10.1016/j.jaridenv.2006.07.006, 2007.4

558 Crow, W. T., Berg, A. A., Cosh, M. H., Loew, A., Mohanty, B. P., Panciera, R., de Rosnay, P., Ryu, D., and Walker, J. P.: Upscaling  
559 sparse ground-based soil moisture observations for the validation of coarse-resolution satellite soil moisture products, *Reviews of*  
560 *Geophysics*, 50, doi:10.1029/2011rg000372, 2012.4

561 Dancy, K., Webster, R., and Abel, N.: Estimating and mapping grass cover and biomass from low-level photographic sampling,  
562 *International Journal of Remote Sensing*, 7, 1679-1704, doi:10.1080/01431168608948961, 1986.4

563 Ding, M. J., Zhang, Y. L., Sun, X. M., Liu, L. S., Wang, Z. F., and Bai, W. Q.: Spatiotemporal variation in alpine grassland phenology in  
564 the Qinghai-Tibetan Plateau from 1999 to 2009, *Chinese Science Bulletin*, 58, 396-405, doi:10.1007/s11434-012-5407-5, 2013.4

565 Dusseux, P., Hubert-Moy, L., Corpetti, T., and Vertes, F.: Evaluation of SPOT imagery for the estimation of grassland biomass,  
566 *International Journal of Applied Earth Observation and Geoinformation*, 38, 72-77, doi:10.1016/j.jag.2014.12.003, 2015.4

567 Fensholt, R., Rasmussen, K., Nielsen, T. T., and Mbow, C.: Evaluation of earth observation based long term vegetation trends—  
568 Intercomparing NDVI time series trend analysis consistency of Sahel from AVHRR GIMMS, Terra MODIS and SPOT VGT data, *Remote*  
569 *sensing of environment*, 113, 1886-1898, 2009.4

570 Gao, X., Huete, A. R., Ni, W., and Miura, T.: Optical-biophysical relationships of vegetation spectra without background contamination,  
571 *Remote sensing of environment*, 74, 609-620, 2000.4

572 Gao, X. X., Dong, S. K., Li, S., Xu, Y. D., Liu, S. L., Zhao, H. D., Yeomans, J., Li, Y., Shen, H., Wu, S. N., and Zhi, Y. L.: Using the  
573 random forest model and validated MODIS with the field spectrometer measurement promote the accuracy of estimating aboveground  
574 biomass and coverage of alpine grasslands on the Qinghai-Tibetan Plateau, *Ecological Indicators*, 112, 106114,  
575 doi:10.1016/j.ecolind.2020.106114, 2020.4

576 Ghosh, S. M. and Behera, M. D.: Aboveground biomass estimation using multi-sensor data synergy and machine learning algorithms in a  
577 dense tropical forest, *Applied Geography*, 96, 29-40, doi:10.1016/j.apgeog.2018.05.011, 2018.4

578 Gitelson, A. A., Kaufman, Y. J., Stark, R., and Rundquist, D.: Novel algorithms for remote estimation of vegetation fraction, *Remote*  
579 *Sensing of Environment*, 80, 76-87, doi:10.1016/s0034-4257(01)00289-9 2002.4

580 Guijarro, M., Pajares, G., Riomoros, I., Herrera, P. J., Burgos-Artizzu, X. P., and Ribeiro, A.: Automatic segmentation of relevant textures  
581 in agricultural images, *Computers & Electronics in Agriculture*, 75, 75-83, doi:10.1016/j.compag.2010.09.013, 2011.4

582 Hague, T., Tillett, N. D., and Wheeler, H.: Automated Crop and Weed Monitoring in Widely Spaced Cereals, *Precision Agriculture*, 7, 21-  
583 32, doi:10.1007/s11119-005-6787-1, 2006.4

584 He, L., Li, A. N., Yin, G. F., Nan, X., and Bian, J. H.: Retrieval of Grassland Aboveground Biomass through Inversion of the PROSAIL  
585 Model with MODIS Imagery, *Remote Sensing*, 11, 1597, doi:10.3390/rs11131597, 2019.4

586 Hoaglin, D. C., Mosteller, F., and Tukey, J. W.: Understanding robust and exploratory data analysis, *Wiley series in probability and*  
587 *mathematical statistics*, 1983.4

588 Holben, B. N.: Characteristics of maximum-value composite images from temporal AVHRR data, *International journal of remote sensing*,  
589 7, 1417-1434, 1986.4

590 Hunt, E. R., Daughtry, C. S. T., Mirsky, S. B., and Hively, W. D.: Remote Sensing With Simulated Unmanned Aircraft Imagery for  
591 Precision Agriculture Applications, *IEEE Journal of Selected Topics in Applied Earth Observations & Remote Sensing*, 7, 4566-4571,  
592 doi:doi:10.1109/jstars.2014.2317876, 2014.4

593 Jiang, W., Yuan, L., Wang, W., Cao, R., Zhang, Y., and Shen, W.: Spatio-temporal analysis of vegetation variation in the Yellow River  
594 Basin, *Ecological Indicators*, 51, 117-126, 2015.4

595 Jiao, C., Yu, G., He, N., Ma, A., and Hu, Z.: The spatial pattern of grassland aboveground biomass and its environmental controls in the  
596 Eurasian steppe, doi:10.11821/dlxb201605007, 2017.4

597 Jibo, Y., Haikuan, F., Xiuliang, J., Huanhuan, Y., Zhenhai, L., Chengquan, Z., Guijun, Y., and Qingjiu, T.: A Comparison of Crop  
598 Parameters Estimation Using Images from UAV-Mounted Snapshot Hyperspectral Sensor and High-Definition Digital Camera, *Remote*  
599 *Sensing*, 10, 1138-, doi:10.3390/rs10071138, 2018.4

600 Kataoka, T., Kaneko, T., Okamoto, H., and Hata, S.: Crop growth estimation system using machine vision, *Advanced Intelligent*  
601 *Mechatronics*, 2003. AIM 2003. Proceedings. 2003 IEEE/ASME International Conference on, Crop growth estimation system using  
602 machine vision,  
603 Kohavi, R.: A study of cross-validation and bootstrap for accuracy estimation and model selection, *Ijcai*, 1137-1145,  
604 doi:10.1109/jstars.2014.2317876,  
605 Li, M., Wu, J., Feng, Y., Niu, B., He, Y., and Zhang, X.: Climate variability rather than livestock grazing dominates changes in alpine  
606 grassland productivity across Tibet, *Frontiers in Ecology and Evolution*, 9, doi:10.3389/fevo.2021.631024, 2021.4  
607 Li, X., Liu, S., Li, H., Ma, Y., Wang, J., Zhang, Y., Xu, Z., Xu, T., Song, L., and Yang, X.: Intercomparison of six upscaling  
608 evapotranspiration methods: From site to the satellite pixel, *Journal of Geophysical Research: Atmospheres*, 123, 6777-6803,  
609 doi:10.1029/2018jd028422, 2018.4  
610 Liu, S., Cheng, F., Dong, S., Zhao, H., Hou, X., and Wu, X.: Spatiotemporal dynamics of grassland aboveground biomass on the Qinghai-  
611 Tibet Plateau based on validated MODIS NDVI, *Scientific reports*, 7, 1-10, doi:10.1038/s41598-017-04038-4, 2017.4  
612 Louhaichi, M., Borman, M. M., and Johnson, D.: Spatially Located Platform and Aerial Photography for Documentation of Grazing  
613 Impacts on Wheat, *Geocarto International*, doi:10.1080/10106040108542184,  
614 Lussem, U., Bolten, A., Menne, J., Gnyp, M. L., Schellberg, J., and Bareth, G.: Estimating biomass in temperate grassland with high  
615 resolution canopy surface models from UAV-based RGB images and vegetation indices, *Journal of Applied Remote Sensing*, 13, 034525,  
616 doi:10.1117/1.Jrs.13.034525, 2019.4  
617 Maimaitijiang, M., Sagan, V., Sidike, P., Maimaitiyiming, M., Hartling, S., Peterson, K. T., Maw, M. J. W., Shakoob, N., Mockler, T., and  
618 Fritschi, F. B.: Vegetation Index Weighted Canopy Volume Model (CVM VI ) for soybean biomass estimation from Unmanned Aerial  
619 System-based RGB imagery, *ISPRS Journal of Photogrammetry and Remote Sensing*, 151, 27-41, doi:10.1016/j.isprsjprs.2019.03.003,  
620 2019.4  
621 Meng, B., Yi, S., Liang, T., Yin, J., and Sun, Y.: Modeling alpine grassland above ground biomass based on remote sensing data and  
622 machine learning algorithm: A case study in the east of Tibetan Plateau, China, *IEEE Journal of Selected Topics in Applied Earth*  
623 *Observations and Remote Sensing*, PP, 1-1, doi:10.1109/Jstars.2020.2999348, 2020.4  
624 Meyer, G. E. and Neto, J. C.: Verification of color vegetation indices for automated crop imaging applications, *Computers and Electronics*  
625 *in Agriculture*, 63, 282-293, doi:10.1016/j.compag.2008.03.009, 2008.4  
626 Michez, A., Piégay, H., Lisein, J., Claessens, H., and Lejeune, P.: Classification of riparian forest species and health condition using multi-  
627 temporal and hyperspatial imagery from unmanned aerial system, *Environmental Monitoring & Assessment*, 188, 1-19,  
628 doi:10.1007/s10661-015-4996-2, 2016.4  
629 Michez, A., Bauwens, S., Brostaux, Y., Hiel, M. P., Garré, S., Lejeune, P., and Dumont, B.: How Far Can Consumer-Grade UAV RGB  
630 Imagery Describe Crop Production? A 3D and Multitemporal Modeling Approach Applied to Zea mays, *Remote Sensing*, 10,  
631 doi:10.3390/rs10111798, 2018.4  
632 Morais, T. G., Teixeira, R. F., Figueiredo, M., and Domingos, T.: The use of machine learning methods to estimate aboveground biomass  
633 of grasslands: A review, *Ecological Indicators*, 130, 108081, doi:10.1016/j.ecolind.2021.108081, 2021.4  
634 Mutanga, O. and Skidmore, A. K.: Narrow band vegetation indices overcome the saturation problem in biomass estimation, *International*  
635 *journal of remote sensing*, 25, 3999-4014, 2004.4  
636 Mutanga, O., Adam, E., and Cho, M. A.: High density biomass estimation for wetland vegetation using WorldView-2 imagery and random  
637 forest regression algorithm, *International Journal of Applied Earth Observation and Geoinformation*, 18, 399-406,  
638 doi:10.1016/j.jag.2012.03.012, 2012.4  
639 O'Mara, F. P.: The role of grasslands in food security and climate change, *Annals of botany*, 110, 1263-1270, doi:10.1093/aob/mcs209,  
640 2012.4  
641 Ramankutty, N., Evan, A. T., Monfreda, C., and Foley, J. A.: Farming the planet: 1. Geographic distribution of global agricultural lands in  
642 the year 2000, *Global biogeochemical cycles*, 22, doi:10.1029/2007GB002952, 2008.4  
643 Saberioon, M. M., Amin, M., Anuar, A. R., Gholizadeh, A., Wayayok, A., and Khairunniza-Bejo, S.: Assessment of rice leaf chlorophyll  
644 content using visible bands at different growth stages at both the leaf and canopy scale, *International Journal of Applied Earth*  
645 *Observations & Geoinformation*, 32, 35-45, doi:10.1016/j.jag.2014.03.018, 2014.4  
646 Suttie, J. M., Reynolds, S. G., and Batello, C.: Grasslands of the World, *Food & Agriculture Org.*2005.  
647 Tan, K., Ciaias, P., Piao, S., Wu, X., Tang, Y., Vuichard, N., Liang, S., and Fang, J.: Application of the ORCHIDEE global vegetation model  
648 to evaluate biomass and soil carbon stocks of Qinghai-Tibetan grasslands, 2010.4  
649 Tucker, C. J.: Red and photographic infrared linear combinations for monitoring vegetation, *Remote Sensing and Environment*, 8, 127-150,  
650 doi:10.1016/0034-4257(79)90013-0, 1979a.4  
651 Tucker, C. J.: Red and photographic infrared linear combinations for monitoring vegetation, *Remote sensing of Environment*, 8, 127-150,  
652 1979b.4  
653 Vergara, J. R. and Estévez, P. A.: A review of feature selection methods based on mutual information, *Neural computing and applications*,  
654 24, 175-186, doi:10.1007/s00521-013-1368-0, 2014.4

655 Viljanen, N., Honkavaara, E., Näsi, R., Hakala, T., Niemeläinen, O., and Kaivosoja, J.: A novel machine learning method for estimating  
656 biomass of grass swards using a photogrammetric canopy height model, images and vegetation indices captured by a drone, *Agriculture*, 8,  
657 70, doi:10.3390/agriculture8050070, 2018.4

658 Wang, J. and Sun, W.: Multiscale geostatistical analysis of sampled above-ground biomass and vegetation index products from HJ-1A/B,  
659 Landsat, and MODIS, *Land Surface Remote Sensing II*, 92601T, 10.1117/12.2069008,

660 Wang, J., Ge, Y., Song, Y., and Li, X.: A geostatistical approach to upscale soil moisture with unequal precision observations, *IEEE*  
661 *Geoscience and Remote Sensing Letters*, 11, 2125-2129, doi:10.1109/Lgrs.2014.2321429, 2014.4

662 Wang, J., Xiao, X., Bajgain, R., Starks, P., Steiner, J., Doughty, R. B., and Chang, Q.: Estimating leaf area index and aboveground  
663 biomass of grazing pastures using Sentinel-1, Sentinel-2 and Landsat images, *ISPRS Journal of Photogrammetry and Remote Sensing*, 154,  
664 189-201, doi:10.1016/j.isprsjprs.2019.06.007, 2019.4

665 Wang, L. a., Zhou, X., Zhu, X., Dong, Z., and Guo, W.: Estimation of biomass in wheat using random forest regression algorithm and  
666 remote sensing data, *The Crop Journal*, 4, 212-219, doi:10.1016/j.cj.2016.01.008, 2016.4

667 Wang, Y., Shen, X., Jiang, M., Tong, S., and Lu, X.: Spatiotemporal change of aboveground biomass and its response to climate change in  
668 marshes of the Tibetan Plateau, *International Journal of Applied Earth Observation and Geoinformation*, 102, 102385, 2021.4

669 Wang, Y., Wu, G., Deng, L., Tang, Z., Wang, K., Sun, W., and Shangguan, Z.: Prediction of aboveground grassland biomass on the Loess  
670 Plateau, China, using a random forest algorithm, *Scientific reports*, 7, 1-10, doi:10.1038/s41598-017-07197-6, 2017.4

671 Woebbecke, D. M., Meyer, G. E., Bargaen, K. V., and Mortensen, D. A.: Color Indices for Weed Identification Under Various Soil,  
672 Residue, and Lighting Conditions, *Transactions of the Asae*, 38, 259-269, doi:10.1109/jstars.2014.2317876 1995.4

673 Woebbecke, D. M., Meyer, G. E., Von Bargaen, K., and Mortensen, D. A.: Plant species identification, size, and enumeration using  
674 machine vision techniques on near-binary images, *Optics in Agriculture and Forestry*, 208-219, 10.1117/12.144030

675 Xia, J., Ma, M., Liang, T., Wu, C., Yang, Y., Zhang, L., Zhang, Y., and Yuan, W.: Estimates of grassland biomass and turnover time on  
676 the Tibetan Plateau, *Environmental Research Letters*, 13, 014020, doi:10.1088/1748-9326/aa9997, 2018.4

677 Yang, S., Feng, Q., Liang, T., Liu, B., Zhang, W., and Xie, H.: Modeling grassland above-ground biomass based on artificial neural  
678 network and remote sensing in the Three-River Headwaters Region, *Remote Sensing of Environment*, S0034425717304741,  
679 doi:10.1016/j.rse.2017.10.011, 2017.4

680 Yang, Y., Fang, J., Pan, Y., and Ji, C.: Aboveground biomass in Tibetan grasslands, *Journal of Arid Environments*, 73, 91-95,  
681 doi:10.1016/j.jaridenv.2008.09.027, 2009.4

682 Yang, Y., Fang, J., Ma, W., Guo, D., and Mohammad, A.: Large-scale pattern of biomass partitioning across China's grasslands, *Global*  
683 *Ecology and Biogeography*, 19, 268-277, doi:10.1111/j.1466-8238.2009.00502.x, 2010.4

684 Yi, S.: FragMAP: a tool for long-term and cooperative monitoring and analysis of small-scale habitat fragmentation using an unmanned  
685 aerial vehicle, *International Journal of Remote Sensing*, 38, 2686-2697, doi:10.1080/01431161.2016.1253898, 2017.4

686 Yu, R., Yao, Y., Wang, Q., Wan, H., Xie, Z., Tang, W., Zhang, Z., Yang, J., Shang, K., and Guo, X.: Satellite-Derived Estimation of  
687 Grassland Aboveground Biomass in the Three-River Headwaters Region of China during 1982–2018, *Remote Sensing*, 13, 2993,  
688 doi:10.3390/rs13152993, 2021.4

689 Zeng, N., Ren, X., He, H., Zhang, L., Zhao, D., Ge, R., Li, P., and Niu, Z.: Estimating grassland aboveground biomass on the Tibetan  
690 Plateau using a random forest algorithm, *Ecological Indicators*, 102, 479-487, doi:10.1016/j.ecolind.2019.02.023, 2019.4

691 Zhang, B., Zhang, L., Xie, D., Yin, X., Liu, C., and Liu, G.: Application of synthetic NDVI time series blended from Landsat and MODIS  
692 data for grassland biomass estimation, *Remote Sensing*, 8, 10, doi:10.3390/rs8010010, 2016.4

693 Zhang, H., Sun, Y., Chang, L., Qin, Y., Chen, J., Qin, Y., Du, J., Yi, S., and Wang, Y.: Estimation of grassland canopy height and  
694 aboveground biomass at the quadrat scale using unmanned aerial vehicle, *Remote sensing*, 10, 851, doi:10.3390/rs10060851, 2018.4

695 Zhang, H. F., Tang, Z. G., Wang, B. Y., Meng, B. P., Qin, Y., Sun, Y., Lv, Y. Y., Zhang, J. G., and Yi, S. H.: A non-destructive method  
696 for rapid acquisition of grassland aboveground biomass for satellite ground verification using UAV RGB images, *Global Ecology and*  
697 *Conservation*, 33, e01999, doi:10.1016/j.gecco.2022.e01999, 2022a.4

698 ZHANG, X., LI, M., WU, J., HE, Y., and NIU, B.: Alpine Grassland Aboveground Biomass and Theoretical Livestock Carrying Capacity  
699 on the Tibetan Plateau, *Journal of Resources and Ecology*, 13, 129-141, 2022b.4

700 Zhang, Y., Bingyu, L. I., and Zheng, D.: Datasets of the boundary and area of the Tibetan Plateau, *ACTA GEOGRAPHICA SINICA*, 69,  
701 164-168, 2014.4

702 Zhang, Y. Q., Tang, Y. H., and Jiang, J. A.: Characterizing the dynamics of soil organic carbon in grasslands on the Qinghai-Tibetan  
703 Plateau, 2007.4

704 Zheng, D.: Natural region system research of Tibetan Plateau, *Science in China (Series D)*, 26, 336–334, 1996.4

705

706